Department of Construction Sciences
Solid Mechanics

ISRN LUTFD2/TFHF-12/XXXX-SE(1-YY)

Experimental study of a dielectric elastomer

Master's Dissertation by

Mujtaba Al-ibadi

Supervisor:
Associate Professor Stephen Hall, Division of Solid Mechanics

Examiner:
Professor Matti Ristinmaa, Division of Solid Mechanics

Printed by Media-Tryck AB, Lund, Sweden
For information, adress:
Division of Solid Mechanics, Lund University, Box 118, SE-221 00 Lund, Sweden
Webpage: www.solid.lth.se

Preface

I am very grateful to have been given the opportunity to work with such an interesting and inspirational project. I would like to thank a few persons that contributed in various ways to this thesis: Stephen Hall, who was supportive and gave valuable feedback throughout the work; Matti Ristinmaa who showed great interest in the project and also gave valuable feedback; Jonas Engqvist, for his assistance and technical expertise during the experiments; Sara Thylander, for her assistance during the experiments as well as providing me with some insight in modelling aspects; I would also like to thank the technician Zivorad Zivkovic without whom, the experiments would not have been possible. I am also grateful for the beam time and support at the MAX IV laboratory.

Abstract

A number of different experiments on a dielectric elastomer, VHB 4910, were performed: uniaxial tensile strain tests, in situ SAXS/WAXS measurements of a sample under uniaxial tensile loading and DIC measurements of an electrically loaded circular sample with simultaneous force measurements around the circular boundary using a novel method developed in this thesis. The results are presented and analysed mainly from an experimental perspective. The results from the WAXS measurements indicate subtle structure change and anisotropy as a result of uniaxial straining. The results from the simultaneous DIC and circular force measurements indicate this to be a promising way of studying electromechanical behaviour of dielectric elastomers. Suggestions are made for future experiments towards refining the method and addressing possible sources of error in the experimental procedure.

Contents

Chapter 1

Introduction

1.1 Purpose and constraints

In this thesis VHB 4910, a dielectric elastomer, is studied using different experiments. The main purpose of this thesis was to develop a setup that allows electromechanical characterization using in situ SAXS/WAXS measurements with simultaneous DIC measurements of an electrically loaded dielectric elastomer. The results are analysed mainly from an experimental perspective, where the data are analysed in terms of the accuracy and precision of the experiments. This is in contrast to typical experimental articles found in the literature, where the data are analysed in terms of the mechanical behaviour and related to a model. While the goal of the experiments is ultimately to understand the material behaviour and develop better models, the time frame of the thesis did not allow for such an analysis.

The aim is that this thesis can serve as a basis for detailed experiments that allows multi-scale characterization of the electromechanical behaviour of dielectric elastomers.

1.2 Structure of thesis

The thesis starts with a short introduction to dielectric elastomers in chapter 2. In chapter 3 the theory behind the experimental methods are explained. A novel method that allows the measurement of forces around a circular boundary is presented separately in chapter 4. In chapter 5 the details of the experiments and sample preparation are presented. The results, followed by a discussion, for each method is presented in chapter 6. Finally, in chapter 7, what has been learnt in this thesis and what can be done in the future are presented.

1.3 Electroactive polymers

Dielectric elastomers fall under the wide category of electroactive polymers (EAP), which are a class of polymers that deform in the presence of an electric field or electric current. There has been an increasing interest in the use of EAP as actuators. They

have a potential to be used in a number of different fields, such as microrobotics, as EAPs are easily scalable, and also in biomimetics, which is why EAPs are often termed artificial muscle. There are a number of different actuation mechanisms and they can be broadly divided into ionic EAPs and electric EAPs. For a survey of the most common actuation mechanisms see Brochu and Pei [1].
One of the most promising types of EAPs are dielectric elastomers, which are capable of producing large displacements suitable in actuators. The interest of this thesis lies within dielectric elastomers, which fall under the electric EAP category. The mechanism by which dielectric elastomers actuates will be presented in chapter 2.

Chapter 2

Dielectric elastomers

A dielectric medium is characterized by two properties, the first property is that it is non-conductive and secondly that it has the ability to polarize in the presence of an electric field. Elastomers are a class of polymers that have a totally elastic behaviour, in other words, they do not show any plasticity. Dielectric elastomers were discovered in the early 1990 [2] and have been under great interest during the last two decades.

The simplest configuration of a dielectric elastomer actuator (DEA) consists of a elastomeric film sandwiched between two electrodes. When a voltage is applied over the electrodes an electric field is created over the film, which causes the film to contract in thickness and expand in the planar direction. There are two phenomena responsible for the deformation of the material. The first is the Maxwell effect, which is generally believed to be the dominating effect in most materials. The other phenomena is the true electrostriction effect. A DEA is essentially a capacitor, and therefore, we will first look at the capacitor and then continue with explaining the Maxwell effect and the true electrostriction effect.

2.1 The capacitor

A simple capacitor consists of a dielectric medium sandwiched between two electrodes. When a voltage is applied over the electrodes an electric field is created that causes an accumulation of charged particles on either side of the dielectric medium. The electric field is directed from the positively charged plate to the negatively charged plate. The simplest geometry of a capacitor is the parallel-plate capacitor where the electrodes are assumed to have a rectangular shape. The capacitance C is used to quantify how well a capacitor can store charged particles [3]:

$$C = \frac{Q}{V}, \tag{2.1}$$

where Q is the stored charge with the unit of Coulomb and V is the applied voltage. For the parallel-plate example the equation reads:

$$C = \epsilon \frac{A}{l}, \tag{2.2}$$

where ϵ is called the permittivity and is a material property of the dielectric medium, A is the area of the plates and l is the distance between them. Instead of the permittivity the so-called dielectric constant is often used, which is defined as the ratio between the permittivity of the dielectric medium and the permittivity of vacuum, ϵ_0:

$$\epsilon_r = \frac{\epsilon}{\epsilon_0}. \tag{2.3}$$

2.2 Maxwell effect

When a voltage is applied over a dielectric material no current will flow through the material, but there will be a separation of charged particles. Positively charged particles will move in the direction of the electric field while negatively charged particles will move in the opposite direction. As a result, there will be an accumulation of opposite charges on either side of the dielectric film. The oppositely charged particles will attract each other and the like charges on each electrode will repel each other. This results in Coloumbic forces that compress the elastomer in the thickness direction and expands the film in the planar direction, see Figure 2.1. Since elastomers are nearly incompressible the contraction in thickness will also lead to significant expansion in the film plane.

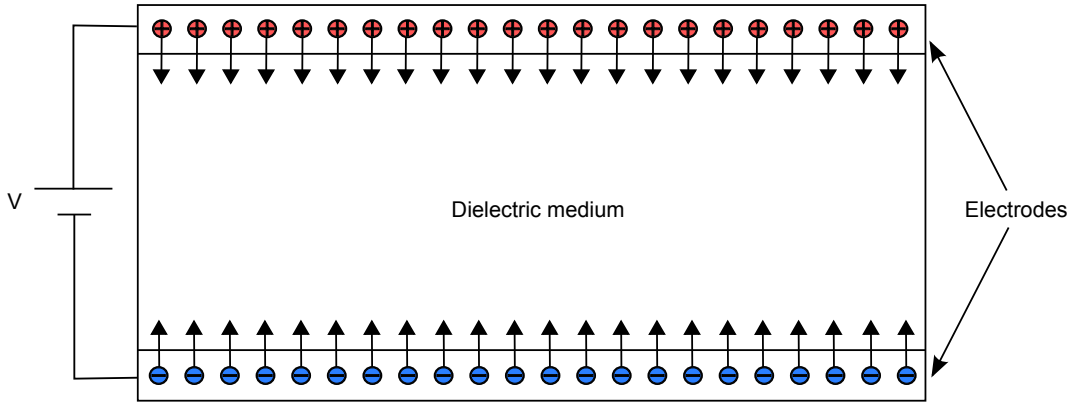

Figure 2.1: Schematic drawing of the Maxwell effect. The drawing shows the attractive forces between the two plates which compresses the dielectric material. Note that there are repulsive forces on the like charges on each electrode which are not shown. The repulsive forces contribute in the expansion of the dielectric material in the planar direction.

The pressure exerted on the elastomer film due to the Maxwell effect is given by the following expression:

$$p_M = \epsilon_0 \epsilon E^2, \tag{2.4}$$

where E is the magnitude of the electric field. We see that the pressure is proportional to the square of the electric field. See Pelrine et al. (1988)[4] for a derivation of this expression.

2.3 True electrostriction effect

While often neglected, there is a second phenomena that causes the elastomer to deform. In some materials, permanent dipoles exist that are randomly oriented, but in the presence of an electric field they align in the direction of the field. This creates attractive forces between the dipoles that causes a contraction of the film in the thickness direction, see Figure 2.2. This phenomena is referred to as ”true electrostriction”[5] or ”inherent electrostriction”[6]. This effect is non-existent in many polymers, but has been found to be the dominating effect in some polymers, such as the polymer family called SEBS [7].

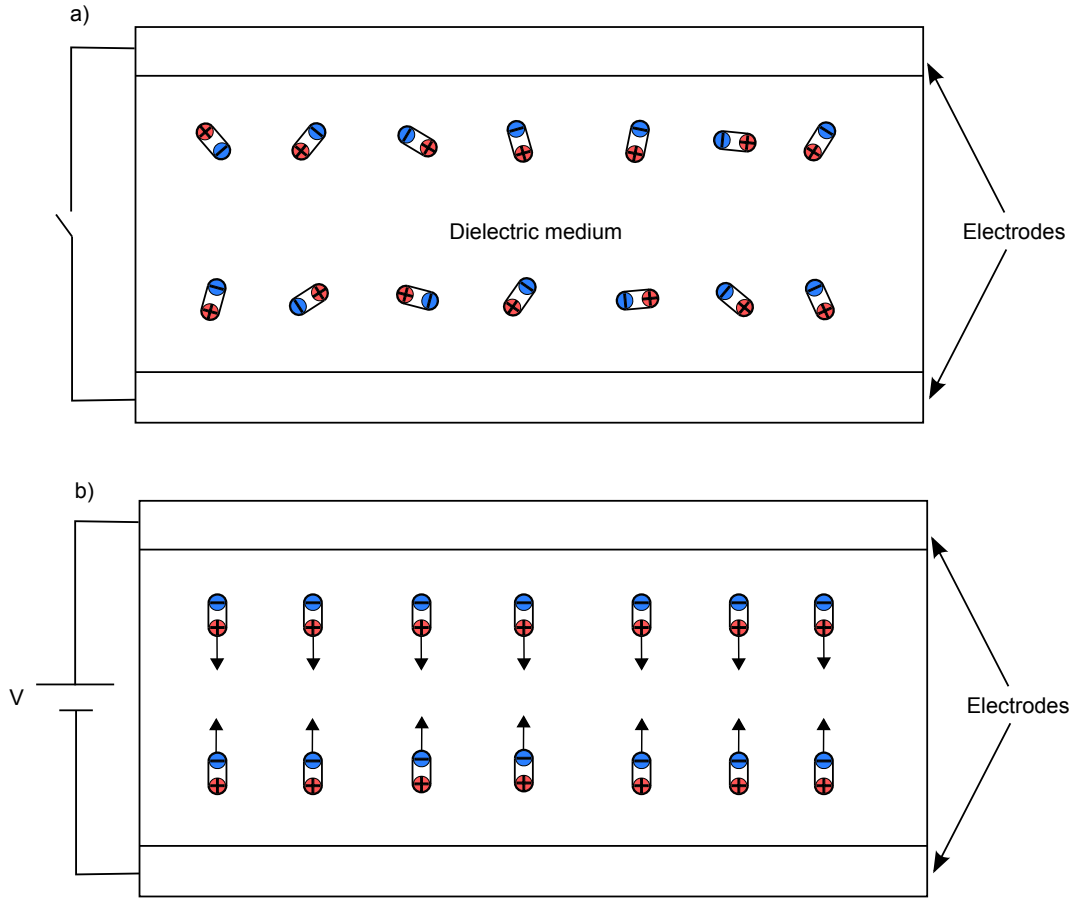

Figure 2.2: Schematic drawing showing the true electrostriction effect. a) There is no electric field over the dielectric material and the dipoles are randomly oriented. b) When a voltage is applied, the dipoles align themselves along the created electric field resulting in attractive forces between the dipoles.

2.4 Failure modes

Aside from mechanical failure, DEAs can fail by two other mechanisms, namely by breakdown failure and by the pull-in instability [8]. When a dielectric medium is

subjected to a large electric field, a portion of the material may become conductive and electrons will flow from one electrode to the other. The conduction can either be momentary or continuous. This can result in permanent damage to the material such as burning or melting due to the high energy of the current. The largest electric field that can be applied before breakdown occurs is called the dielectric strength and is an important material property.

Pull-in instability is a failure mechanism that occurs when the compressive pressure exceeds the internal stress of the elastomer, which causes the elastomer film to compress. Because the electric field is the applied voltage divided by the distance between the electrodes, there will be an increase in the electric field. This further increases the compressive pressure causing a chain reaction where the film gets increasingly thinner and eventually leads to the failure of the material, either by mechanical failure or dielectric breakdown.

2.5 Effects of pre-strain

In an article by Pelrine et al. (2000) [9] it was shown that pre-straining the elastomer film had a significant effect on the actuation performance. They measured electrically actuated strains up to 215% for an acrylic elastomer. This enhanced response can be attributed to a number of explanations. In an article by Su et al. (1997)[10], they discovered that thinner films of polyurethane reached larger actuation strains compared to thicker films exposed to the same electric field. It was suggested that the enhanced response of thinner films is a geometrical effect. In a study of VHB 4910, Kofod et al. (2003) [11] showed that pre-straining the elastomer increased the dielectric strength and thus, the enhanced actuation is simply due to the fact that a higher electric field can be applied.

2.6 Electrodes

The electrodes used in a DEA need to be compliant and be able to maintain conductivity at large strains. There are several materials that can be used as electrodes. The most common are carbon-based electrodes. They can be applied in powder form consisting of either carbon black or graphite powder. The powder can also be mixed with a viscous oil to make a conductive grease. Carbon-based electrodes provide sufficient conductivity while having no impact on the stiffness of the elastomer and is the most common choice of electrodes in the literature [12]. A disadvantage with powder-based electrodes is that they are hard to apply in a desired shape.

2.7 DEA material

Most polymers are dielectric, however, there are some polymers that are more suitable to be used as DEAs. As mentioned, two important material properties are the dielectric constant and the dielectric strength, these two properties should be as large

as possible. Additionally, the mechanical properties also play a roll, for instance, polymers with highly viscous response are typically unwanted. A number of different polymers have been investigated in terms of their potential to be used as a DEA. These include: rubbers, silicones, polyurethanes, acrylics and a group of polymers termed electroactive nanostructured polymers (ENPs). For a comparison of different dielectric polymers see Shankar et al. 2007 [13]. Two polymers that stand out are the commercially available acrylic manufactured by 3M^{TM} called VHB^{TM} 4910 and the commercially available ENP from Kraton^{TM} called SEBS. These two polymers have been reported to show the largest actuation strains.

2.8 VHB 4910

VHB 4910 belongs to the group of polymers termed acrylics. Acrylic polymers are known for their optical transparency and resistance to weathering [3]. VHB 4910 is a double sided tape and is advertised to be used in a wide number of applications, for instance, the tape can be used as joints in building constructions. The tape is available in two thickness's: 1 mm and 0.5 mm. The 1 mm thick tape is marketed as VHB 4910 while the 0.5 mm thick tape is marketed as VHB 4905. They come in a wide number of sizes, either as rolls or sheets.

The mechanical and electromechanical behaviour of this material has been studied in a number of articles (e.g. [14, 15, 16, 11, 9]).

The micro structure of VHB 4905 along with three other acrylics was studied by Stenzler & Goulbourne (2011) [17] using a stereo microscope, they found that VHB 4905 had no discernible micro structure, see Figure 2.3.

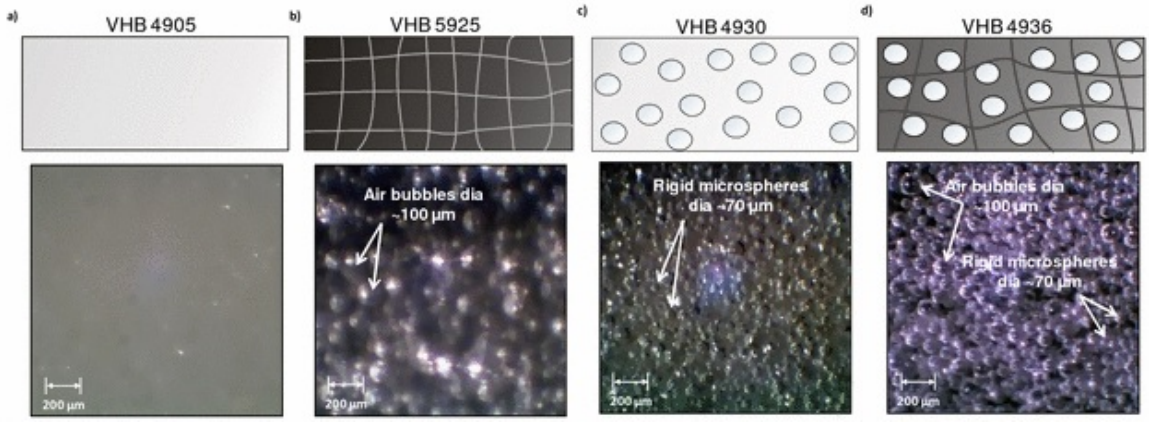

Figure 2.3: Micro structure of four acrylics from 3M. From [17].

Chapter 3

Experimental methods

Two types of experiments were performed for this thesis:

- In situ SAXS/WAXS measurements of a rectangular sample under tensile load.
- Simultaneous DIC and force measurements of an electrically loaded circular sample.

This sections presents the theory behind the methods and the used definitions. The method by which the forces of the circular sample were measured is presented in a separate chapter.

3.1 Uniaxial tensile tests

Conventional uniaxial tensile tests were performed to determine the stress-strain response of VHB 4910. The tests were displacement controlled. Since the studied material shows pronounced visco-elastic behaviour, two displacement rates were tested, one very slow, to get the quasi-static response, and one fast rate, which is more representative of the electrically loaded case. The stress is calculated using the definition of nominal stress:

$$\sigma = \frac{F}{A_0}, \tag{3.1}$$

where A_0 is the initial cross section area. The strain is calculated using the definition of engineering strain:

$$\varepsilon = \frac{l}{l_0} - 1. \tag{3.2}$$

3.2 X-ray scattering

In this work SAXS and WAXS is used to study the molecular structure of VHB 4910. This section describes the background to X-ray scattering. The discussion starts with the case of X-ray diffraction to outline the basic concept and followed by how this concept is implemented in SAXS and WAXS.

Electromagnetic waves with wavelengths between about 10^{-8} to 10^{-11} m are conventionally considered to be X-rays. A common unit used in relation with material studies at the atomic level is Ångström(Å, 10^{-10}m). Typically the wavelength used with X-ray diffraction is in the region of 0.5-2.5 Å [18]. X-rays are used to probe structures at a very small scale. By studying the scattering that is created when a material is illuminated by a X-ray beam it is possible to draw conclusions about the material structure.

3.2.1 Interaction of X-rays with matter

There are several in ways which electromagnetic waves can interact with matter. These can be divided into two categories: absorption and scattering. Absorption can be defined as the reduction in flux (transmitted energy per area per second) and scattering can be defined as the change of direction of the incident beam. The interactions that lead to absorption are of interest when using X-ray imaging techniques and are unwanted in X-ray diffraction methods. The main interaction of interest in relation with X-ray scattering techniques is the so-called Thomson scattering. This interaction occurs when the electric field of an incident X-ray beam accelerates the electrons in the material so that the electrons will vibrate with same frequency as the incident beam. This vibration causes emission of photons with the same frequency and wavelength as the incident photons. The emitted photons propagate in all directions creating spherical waves, see Figure 3.1.

There are two important properties of Thomson scattering. The first is that the scattering is elastic, which means that the scattered photons do not lose any energy in the process, equivalently, this means that the wavelengths of the scattered photons are the same as wavelength of the incident photons. The second property is that the scattering is coherent, meaning that the scattered photons are synchronized, or in other words; there are no phase shifts between them. These two properties make it possible for the scattered waves to produce diffraction patterns.

Another occurring scattering interaction is called Compton scattering. This occurs when energy from the photon is partially passed to an electron resulting in a scattered photon with less energy. This scattering is inelastic and incoherent and gives rise to unwanted noise when only coherent scattering is of interest.

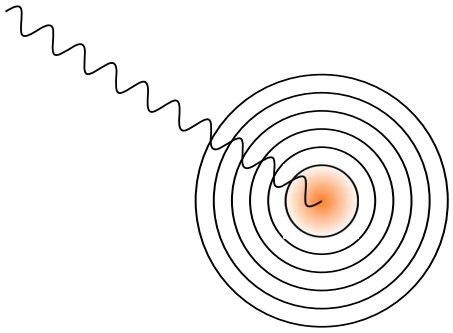

Figure 3.1: Spherical waves produced in a Thomson interaction.

3.2.2 Bragg's law

Consider a Thomson scattering interaction by two atoms separated by the distance d. The direction of the incident beam is given by the angle α, which is defined relative to a line perpendicular to d. The scattering occurs in different directions given by β and is recorded on a detector far away, see Figure 3.2. The direction of the scattered waves relative to the incident beam is given by the angle 2θ which is commonly called the scattering angle [18, 19].

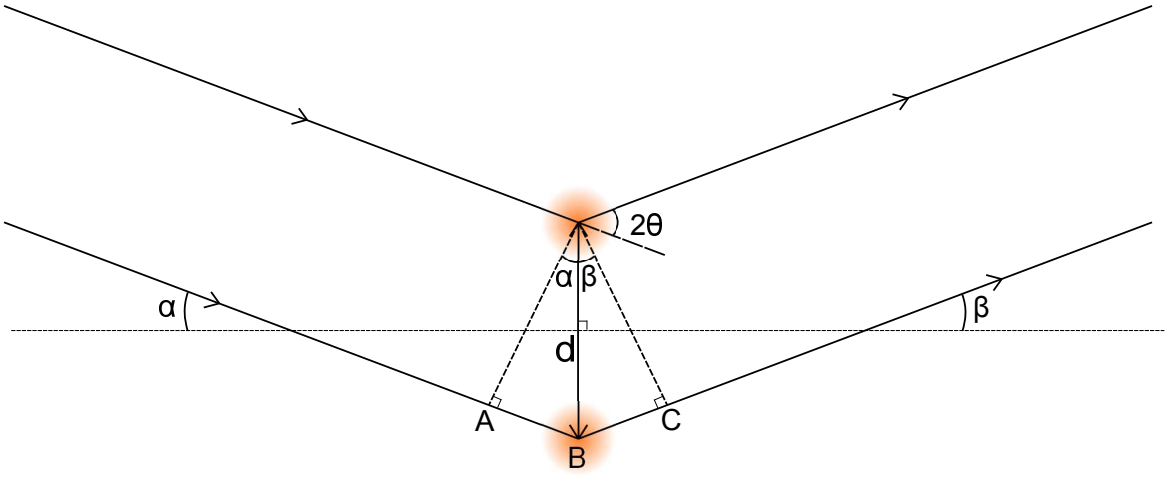

Figure 3.2: Thomson scattering interaction by two atoms.

Since the waves are coherently scattered, the phase difference depends only on the path difference which is given by AB+BC. In order for the waves to constructively interfere, the path difference must be an integer multiple of the wavelength:

$$dsin\alpha + dsin\beta = n\lambda. \tag{3.3}$$

When the angle of the incident waves is the same as the angle for the scattered wave we see that $\alpha = \beta = \theta$ and Equation (3.3) reduces to:

$$2dsin\theta = n\lambda. \tag{3.4}$$

This is known as Bragg's law which was first proposed in 1913 by father and son, Sir William Lawrence Bragg and Sir William Henry Bragg. By studying the intensity of the scattered waves as a function of the scattering angle, it is possible to draw conclusions about the structure of the studied material. Instead of θ it is common to use the so-called q vector to characterize the scattering geometry. The q vector is defined as the difference between the incident and the scattered wave vector. The magnitude of the q vector is given by:

$$q = \frac{4\pi}{\lambda} sin\theta. \tag{3.5}$$

3.2.3 Analysing the diffraction pattern

When the intensity of the diffraction is analysed, certain assumptions must be made in order to make any conclusions about the structure of the material. If the scatterers in a material are far apart from each other, in relation to the wavelength, the diffraction pattern will reveal the so-called form factor. The form factor gives information about the shape and size of the scatterers. The diffraction pattern produced by a dilute material with simple geometric shapes is characterised by an oscillating intensity, see Figure 3.3.

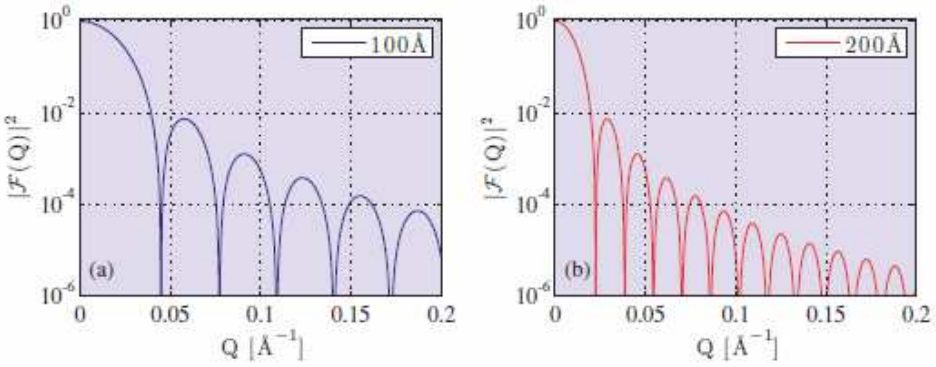

Figure 3.3: Form factor of spheres with two different radii, 100 Å and 200 Å. From [19]

For a diffraction pattern to reveal the form factor the distances between the particles must be much larger than the wavelength. Also, the material must be monodisperse, which means that the particles are identical in size and shape. If the material is not monodisperse, the diffraction pattern will instead give an average form factor with less pronounced minima [20].

When the distances between the particles are in the same order of magnitude as the wavelength, the scattering from the particles will interfere and produce a diffraction pattern that can reveal information about the structure of the material. In the case of crystalline material, the interference will produce sharp intensity peaks at certain scattering angles, commonly referred to as Bragg peaks. The position of the peaks described as a function of the scattering angle or q, can then be used to calculate distances (d-spacings) between atomic planes using Bragg's law:

$$d = \frac{2\pi}{q}. \tag{3.6}$$

In the case of amorphous materials, such as glass and liquids, the interference will produce broad peaks that can reveal information about the short-range structure.

Typically a large number of scatterers are illuminated and the diffraction pattern will be a sum of the scattering from all scatterers. For a material with a well ordered structure where the scatterers are all identically oriented, the diffraction pattern recorded on a 2D detector will have well defined spots at certain azimuth angles. If the scatterers are differently oriented the diffraction pattern will contain many spots

corresponding to the different orientation angles. For a material where there is a random distribution of orientations the diffraction pattern will produce so-called powder rings.

To determine the position of the peaks it is possible to simply look at the scattering angle where the highest intensity is. However, it is recommended to fit appropriate distribution models and extract the peak position from the model parameter. A Gaussian distribution can often be fitted to the intensity as a function of scattering angle. This does not always produce good fits and it is sometimes suitable to add a linear or exponential background term. The tails of the Gaussian are often the regions where the fitting is worst, and to solve this, a Lorentzian term can be added [21]. The equation for the Gaussian distribution is given by:

$$I(q) = ae^{-\left(\frac{q-b}{c}\right)^2}, \tag{3.7}$$

where a is the amplitude, b is the centroid and c is related to the peak width.

Using Equation 3.6 together with the definition of engineering strain (Equation 3.2), a strain related to the peak positions can be formulated:

$$\varepsilon_q = \frac{q_0}{q} - 1. \tag{3.8}$$

3.2.4 SAXS and WAXS

Small angle X-ray scattering (SAXS) and wide angle X-ray scattering (WAXS) are two methods that utilize the concept outlined above. But, rather than the scattering between atomic planes, these methods are used to study scattering of larger structures. The scattering measured with SAXS and WAXS is from clusters of atoms. As such, to detect any structure, the particles of interest must have a contrasting electron density in relation to its surroundings.

With SAXS, the intensities are recorded at small scattering angles, $2\theta = 0.1\,° - 10\,°$, allowing the study of features larger than 10 Å[18]. With wide angle X-ray scattering (WAXS), the intensity is recorded at larger scattering angles compared to SAXS, which allows the measurements of smaller features. The two methods rely on the same theory and reveal similar information. In practice the difference between SAXS and WAXS is the distance of the sample to the detector. With WAXS, the detector is placed closer to the sample which allows the detection of scattering at wider angles. Although the shorter angles are also recorded with WAXS, it is preferred to use SAXS for smaller angles to get a better resolution in the small angle region.

3.3 3D-surface digital image correlation

Digital image correlation (DIC) is a non-contact method that is used to measure the displacement field of a deforming sample. This method relies on the comparison of two images and tracks how predefined points change from one image to another. This is accomplished by comparing segments from one image to another image at a different

time. Assuming that a segment is unique and that this uniqueness can be quantified, it should be possible to identify the segment in both photos, even if it changes position. These segments consist of neighbourhoods of pixels, commonly called subsets. The uniqueness of the subset is characterized by the grey-scale values of the pixels in the subset. There are different ways of calculating how well two subsets match, a basic criteria is given by the sum of squared deviations [22]:

$$SSD = \sum (I_2(\mathbf{x} + \mathbf{d}) - I_1(\mathbf{x}))^2, \tag{3.9}$$

where I_1 and I_2 are the grey-scale values of the reference image and the deformed image at the pixel position $\mathbf{x}$ and $\mathbf{x}$+$\mathbf{d}$. The objective is to find the displacement $\mathbf{d}$ that gives the minimum value of the SSD.

With the matching algorithm above the subset is assumed to retain its shape, however if the subsets are not small enough they might undergo deformation or rotation, which would cause a bad correlation. To account for deformation and rotation it is possible to transform the subsets in the second image by a shape function [22].

Between two images some change in intensity is inevitable, which introduces an error to the correlation. The change in intensity may be due to the sample changing its orientation and thus the reflected light detected by the camera changes. It could also be due to changes in texture or simply a change in lighting. In the case of stereo correlation where images are compared from two different cameras the problem of difference in intensity is even more present. To deal with this issue, a number of different correlation criteria are available. One is the normalised cross correlation criterion:

$$NCC = \frac{\sum I_1(\mathbf{x}) I_2(\mathbf{x} + \mathbf{d})}{\sqrt{\sum I_1(\mathbf{x})^2 \sum I_2(\mathbf{x} + \mathbf{d})^2}} \tag{3.10}$$

The advantage of the NCC criteria is that it is independent of scale [22], that is, between two images I_1 and I_2 the criteria will give accurate result even if the intensity of I_2 is different by a factor. The criteria used in this report is the normalized sum of squared deviations, which is also independent of scaling:

$$NSSD = \sum \left(\frac{\sum I_1(\mathbf{x}) I_2(\mathbf{x} + \mathbf{d})}{\sum I_2(\mathbf{x} + \mathbf{d})^2} I_2(\mathbf{x} + \mathbf{d}) - I_1(\mathbf{x}) \right)^2 \tag{3.11}$$

If the grey-scale values are evaluated at the discrete pixels, the displacement can only assume an integer number of pixels. However, it is possible to obtain sub-pixel resolution by evaluating the grey-scale values of the second image in interpolated positions.

Since we are requiring that there is a unique matching between two subset there are some requirements on the measured surface. The color of the surface can not be homogeneous and there must be some sort of pattern. The pattern should not be periodic and should have no orientation [22]. This is usually accomplished by the application of a so-called speckle pattern.

DIC can be used to track positions in all spatial dimensions, depending on how the measurements are made. The simplest case is measurements made by one camera,

which can measure deformation in two dimensions. This is called 2D-surface DIC and is suitable when the studied object is assumed to only undergo plane deformation. It is also possible to measure three-dimensional deformation using tomography techniques, such as X-ray tomography, which enable the measurement of internal deformation of an object. In this report three-dimensional surface (3D-surface DIC) measurements has been performed using stereo-vision.

When a 3D object is recorded on a 2D detector, information about the third dimension is lost. However, with a stereo-vision system, where images of an object are taken simultaneously by two cameras, information about the third dimension can be retrieved. This is illustrated in Figure 3.4. If the points P_1 and P_2 are only detected by the left camera, they would both be detected in the point r and thus the position along the dotted line is lost. When a second camera is added we see that the 3D position can be determined uniquely by (r, p_1) and (r, p_2) for the points P_1 and P_2, respectively [22].

The image correlation presented in this report was made using the commercial software VIC-3D$^{\text{TM}}$ from Correlated Solutions.

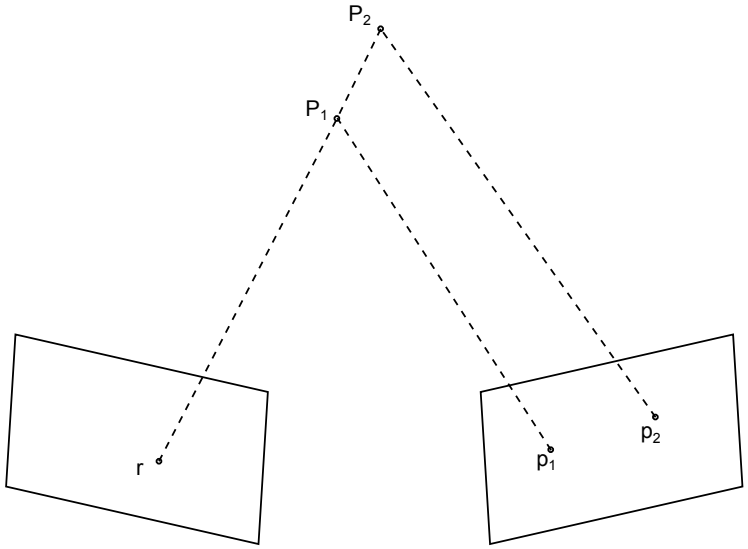

Figure 3.4: Illustration of how 3D position can be determined using stereo-vision. The rectangles represent the detectors of the cameras.

3.3.1 Continuum mechanics

DIC provides the displacement field, which can be used to calculate the strain field using continuum mechanics. In the following, the general theory and its implementation with regard to 3D-surface DIC is presented.

Consider a small line element given by the vector $d\mathbf{r}_0$ that connects two material points in the body β_0 in the reference configuration. This line element undergoes deformation and transforms into a vector denoted $d\mathbf{r}$ in the current configuration, see Figure 3.5.

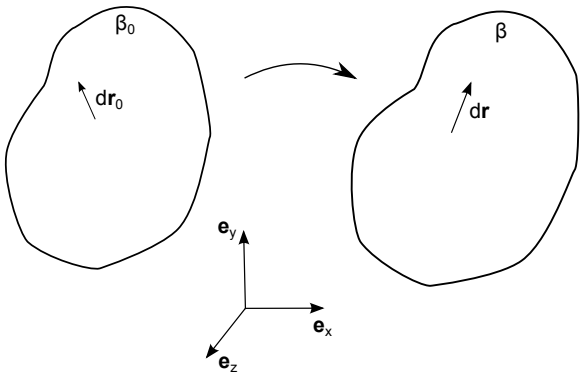

Figure 3.5: A body β_0 in the reference configuration and its transformation to the body β in the current configuration.

The transformation of the line vector from the reference to the current configuration is given by:

$$d\mathbf{r} = \mathbf{F}d\mathbf{r}_0, \tag{3.12}$$

where $\mathbf{F}$ is known as the deformation gradient and has the following components:

$$\mathbf{F} = \begin{bmatrix} \dfrac{\partial x}{\partial x_0} & \dfrac{\partial x}{\partial y_0} & \dfrac{\partial x}{\partial z_0} \\ \dfrac{\partial y}{\partial x_0} & \dfrac{\partial y}{\partial y_0} & \dfrac{\partial y}{\partial z_0} \\ \dfrac{\partial z}{\partial x_0} & \dfrac{\partial z}{\partial y_0} & \dfrac{\partial z}{\partial z_0} \end{bmatrix}. \tag{3.13}$$

Since the deformation is only measured on the surface with 3D-surface DIC, the variation along the thickness is not available and we do not get the components in the third column:

$$\mathbf{F}_{3DS} = \begin{bmatrix} \dfrac{\partial x}{\partial x_0} & \dfrac{\partial x}{\partial y_0} & ? \\ \dfrac{\partial y}{\partial x_0} & \dfrac{\partial y}{\partial y_0} & ? \\ \dfrac{\partial z}{\partial x_0} & \dfrac{\partial z}{\partial y_0} & ? \end{bmatrix}. \tag{3.14}$$

3.3.1.1 Green-Lagrange strain

The strain measurement used in this report is the Green-Lagrange strain,

$$\mathbf{E} = \frac{1}{2}(\mathbf{C} - \mathbf{I}), \tag{3.15}$$

where $\mathbf{C}$ is the right Cauchy-Green's deformation tensor,

$$\mathbf{C} = \mathbf{F}^T\mathbf{F} = \begin{bmatrix} \frac{\partial x}{\partial x_0} & \frac{\partial y}{\partial x_0} & \frac{\partial z}{\partial x_0} \\ \frac{\partial x}{\partial y_0} & \frac{\partial y}{\partial y_0} & \frac{\partial z}{\partial y_0} \\ ? & ? & ? \end{bmatrix} \begin{bmatrix} \frac{\partial x}{\partial x_0} & \frac{\partial x}{\partial y_0} & ? \\ \frac{\partial y}{\partial x_0} & \frac{\partial y}{\partial y_0} & ? \\ \frac{\partial z}{\partial x_0} & \frac{\partial z}{\partial y_0} & ? \end{bmatrix} =$$

$$= \begin{bmatrix} (\frac{\partial x}{\partial x_0})^2 + (\frac{\partial y}{\partial x_0})^2 + (\frac{\partial z}{\partial x_0})^2 & \frac{\partial x}{\partial x_0}\frac{\partial x}{\partial y_0} + \frac{\partial y}{\partial x_0}\frac{\partial y}{\partial y_0} + \frac{\partial z}{\partial x_0}\frac{\partial z}{\partial y_0} & ? \\ \frac{\partial x}{\partial y_0}\frac{\partial x}{\partial x_0} + \frac{\partial y}{\partial y_0}\frac{\partial y}{\partial x_0} + \frac{\partial z}{\partial y_0}\frac{\partial z}{\partial x_0} & (\frac{\partial x}{\partial y_0})^2 + (\frac{\partial y}{\partial y_0})^2 + (\frac{\partial z}{\partial y_0})^2 & ? \\ ? & ? & ? \end{bmatrix}. \quad (3.16)$$

Evidently, the surface DIC measurement only gives four components of the strain tensor (where the shear components are identical):

$$\mathbf{E} = \begin{bmatrix} E_{xx} & E_{xy} & ? \\ E_{yx} & E_{yy} & ? \\ ? & ? & ? \end{bmatrix}, \ \mathbf{E}_{2D} = \begin{bmatrix} E_{xx} & E_{xy} \\ E_{yx} & E_{yy} \end{bmatrix}. \quad (3.17)$$

This is not to be confused with plane deformation, the components in the strain tensor contain contributions from all three dimensions as seen in Equation 3.16.

The principal strains and principal strain directions presented in the result sections are the quantities given by the following eigenvalue problem:

$$\mathbf{E}_{2D}\mathbf{n}_i = \lambda_i\mathbf{n}_i \Leftrightarrow (\mathbf{E}_{2D} - \mathbf{I}\lambda_i)\mathbf{n}_i = \mathbf{0}, \quad i = 1, 2. \quad (3.18)$$

Where λ_i are the principal strains and $\mathbf{n}_i$ are the principal strain directions. Notice that the eigenvalue problem is solved for the two-dimensional strain tensor where the unknown components have been removed. This means that the principal directions will be in the xy-plane and the eigenvalues will be the same as the eigenvalues for the following strain state:

$$\mathbf{E} = \begin{bmatrix} E_{xx} & E_{xy} & 0 \\ E_{yx} & E_{yy} & 0 \\ 0 & 0 & E_{zz} \end{bmatrix}. \quad (3.19)$$

The characteristic equation for 3.19 is given by:

$$det(\mathbf{E} - \mathbf{I}\lambda) = (E_{zz} - \lambda)\underbrace{\left((E_{xx} - \lambda)(E_{yy} - \lambda) - {E_{xy}}^2\right)}_{det(\mathbf{E}_{2D} - \mathbf{I}\lambda)} = 0. \quad (3.20)$$

Where we see that one root is given by $\lambda = E_{zz}$ and the remaining two roots are the same as for Equation 3.18. The strain state is therefore evaluated with the assumption that the shear components E_{xz} and E_{yz} are negligible.

3.3.1.2 Thickness strain and isochoric deformation

The thickness strain is not given directly by the DIC measurements, but can be approximated instead. This can be done in two ways, either with the assumption that the deformation is symmetric around the xy-plane or with the assumption of isochoric deformation. With the former assumption, the deformed thickness is given by

$$t = t_0 + 2W, \tag{3.21}$$

where W is the displacement in the z-direction. The thickness engineering strain is given by

$$\epsilon_t = \frac{t}{t_0} - 1 = \frac{2W}{t_0} \tag{3.22}$$

and the E_{zz} component of the Green Lagrange strain tensor is

$$E_{zz} = \frac{1}{2}\left((\frac{\partial z}{\partial z_0})^2 - 1\right) = \frac{1}{2}\left((\frac{t}{t_0})^2 - 1\right) = 2\left((\frac{W}{t_0})^2 + \frac{W}{t_0}\right). \tag{3.23}$$

The studied polymer is nearly incompressible and, therefore, the assumption of isochoric deformation is justified. This condition is related to the deformation gradient by the Jacobian:

$$\frac{dV}{dV_0} = J = det(\mathbf{F}) = 1. \tag{3.24}$$

With the assumptions made in the previous section the deformation gradient is given by:

$$\mathbf{F} = \begin{bmatrix} \frac{\partial x}{\partial x_0} & \frac{\partial x}{\partial y_0} & 0 \\ \frac{\partial y}{\partial x_0} & \frac{\partial y}{\partial y_0} & 0 \\ \frac{\partial z}{\partial x_0} & \frac{\partial z}{\partial y_0} & \frac{t}{t_0} \end{bmatrix}. \tag{3.25}$$

The Jacobian is then given by

$$J = \frac{t}{t_0} det(\mathbf{F}_{2D}) = 1, \tag{3.26}$$

where

$$\mathbf{F}_{2D} = \begin{bmatrix} \frac{\partial x}{\partial x_0} & \frac{\partial x}{\partial y_0} \\ \frac{\partial y}{\partial x_0} & \frac{\partial y}{\partial y_0} \end{bmatrix}. \tag{3.27}$$

The isochoric condition can also be stated as:

$$\frac{t}{t_0}\frac{dA}{dA_0} = 1 \tag{3.28}$$

We can recognize that $det(\mathbf{F}_{2D})$ gives the area change in the xy-plane, $\frac{dA}{dA_0}$. With the notation $J_{2D} = det(\mathbf{F}_{2D})$ we get the following result:

$$t = \frac{t_0}{J_{2D}},\ \epsilon_t = \frac{1}{J_{2D}} - 1,\ E_{zz} = \frac{1}{2}\left(\frac{1}{J_{2D}^2} - 1\right). \tag{3.29}$$

Chapter 4

Circular boundary force measurements

Most experiments described in the literature for dielectric elastomers only measures a macroscopic deformation and compares this with the electric load. A challenge in this thesis was to develop a setup that measures the forces produced by a electrically loaded elastomer so that it is possible to calculate stresses induced in a sample.

A novel method was developed in this thesis that allows the measurements of forces created around the boundary of a circular sample. A device was built from a plexi glass cylinder where one end of the cylinder was cut into twelve arms. On each of the arms, two strain gauges were attached, one on the inside of the cylinder, and one on the outside. The strain gauges were connected in a half-bridge configuration. See Figure 4.1 for a photo of the device.

The twelve strain gauge bridges was connected to 3 modules of NI 9237 in a NI cDAQ-9178 chassis from National Intruments. The data acquisition was performed using a program developed in LabVIEW. The strain gauge data could be interpreted in terms of the boundary forces given a correct calibration as described in the next section.

This device was also designed to be suitable for in situ SAXS/WAXS measurement as there is nothing that could obstruct a beam going through the sample.

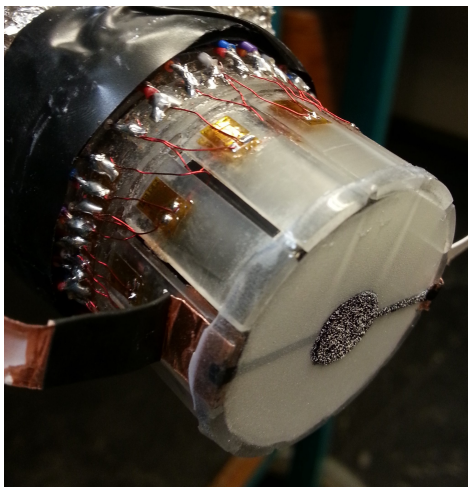

Figure 4.1: The device which measures the forces around a circular boundary

4.1 Calibration

The relationship of the recorded signal from each of the 12 arms was calibrated to provide local force measurements by hanging known weights at the edge. It was assumed that the arms would be subjected to forces in a sufficiently small region so that a linear relationship between the signal and force could be used. This is confirmed by Figure 4.2 that shows the measured signal from hanging 21 different weights, ranging from 40 to 60 g. The linear fit does not intersect the origin, which suggests that the response is non-linear in a bigger region (the signal was zero for no load). The rest of the arms where calibrated by hanging only two weights (30 and 50 g) in order to save time.

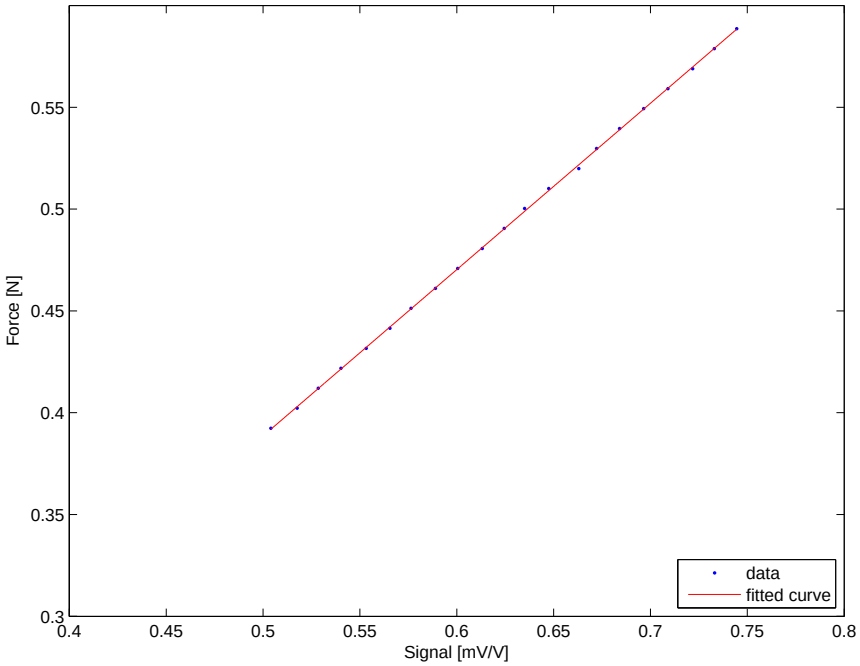

Figure 4.2: The linear relation between the signal and force. The fitted linear equation is given by $0.817 * signal - 0.01991$.

Chapter 5

Experiments

This chapter presents the details of the experiments and the sample preparation.

5.1 Uniaxial tensile tests

The samples were prepared from a roll of 25 mm wide VHB 4910 (1 mm thick) tape. Rectangular 10 x 25 mm samples were cut with the long axis perpendicular to the roll length. Uniaxial strain tests where performed using a custom made device described in [23]. The gap between the grips was 10 mm when the samples were clamped, leaving 7.5 x 10 mm of the tape inside each grip. The clamping process squeezed out material, which buckled the sample and ,therefore, the gap does not represent the initial length, see Figure 5.1. Instead, the initial length was determined experimentally by studying the force-displacement response. The initial length was considered to be the initial gap between the grips plus the displacement at which the force begins to increase, i.e. when the sample starts to stretch.

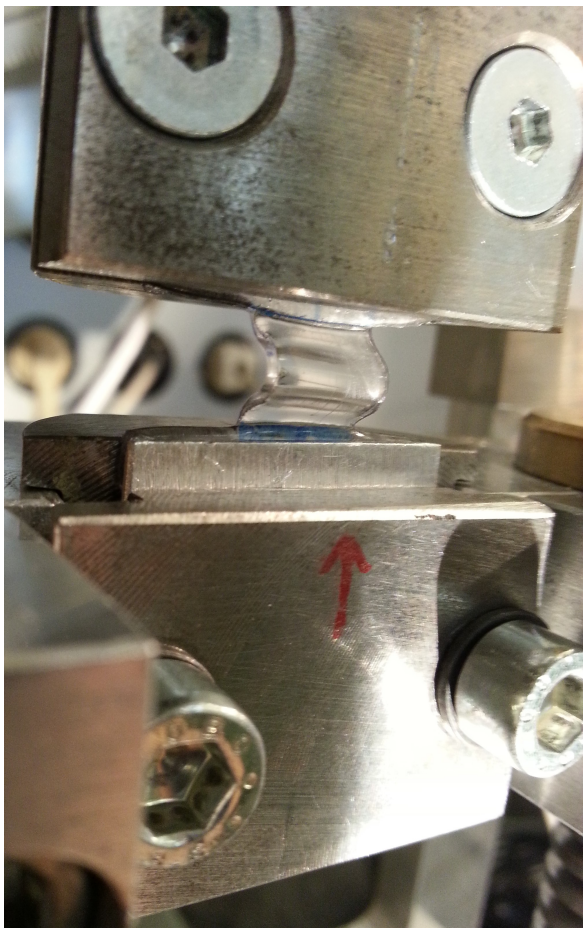

Figure 5.1: Photo showing how the sample buckles when it is clamped

Early experiments showed very inconsistent results. This is believed to be caused by shearing occurring in the interface between the sample and the grips, causing the sample to bend, see Figure 5.2a. As the sample was clamped by screwing two plates by hand, different internal stresses were induced, depending on how hard each sample was clamped. To minimise the shearing effect, small strips of the same VHB tape were attached to the edges of the grip plates, see Figure 5.2b. The tests were displacement controlled and the samples were stretched to failure. Two different displacement rates were used: 5 mm/min and 0.06 mm/min.

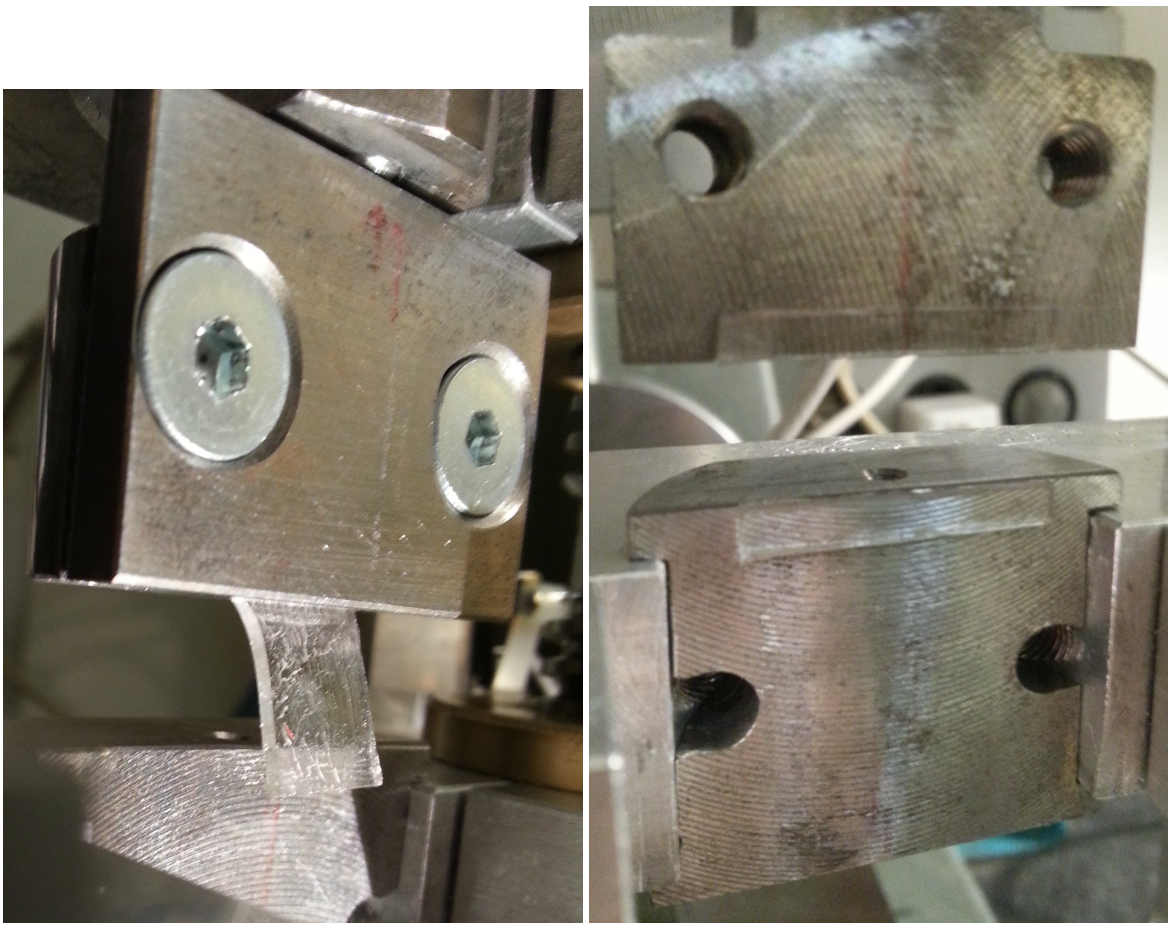

(a) (b)

Figure 5.2: (a) The photo shows how a sample bends as a result of clamping (b) The placement of small strips to reduce the shearing effect.

5.2 WAXS with in situ tensile loading

WAXS with in situ uniaxial tensile loading experiments were performed at the I911-SAXS beamline at MAX IV Laboratory. The same device and sample preparation was used as in previous section. The sample had the same geometry except that it had double thickness, which was accomplished by sticking two samples together. The double thickness was used to provide a stronger WAXS signal. The sample was stretched to failure with a displacement rate of 0.24 mm/min. The long axis (perpendicular to the roll length) of the sample was vertically oriented in the loading device. Unfortunately, the load cell was not working at that time so the force was not measured.

The wavelength of X-rays was 0.91 Å. A sample of silver behenate was used to determine the sample to detector distance as well as determine the center of the beam on the 2D detector. The sample to detector distance was determined to be 0.3751 m. The sample was illuminated in a single point 140 times during the tensile loading

with an exposure time of 60 s.

5.3 Circular samples with electric load

Two samples at different pre-strains were prepared, one with equiaxial pre-strain of 300% and one with 300% in one direction and 200% in the perpendicular direction. To prepare the samples, square pieces (approximately 51 mm wide) were cut with a scalpel from a 4 inch wide roll of VHB 4910 tape. Circles with 10 mm diameter were marked in the center of the square pieces and then biaxially stretched in a simple device, see Figure 5.3.

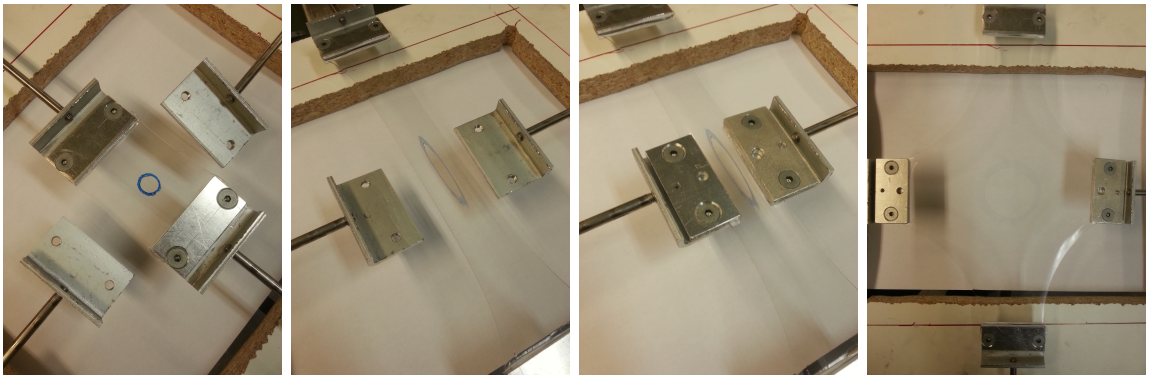

Figure 5.3: The different steps of the biaxial pre-stretch

The sample with equiaxial pre-strain was stretched until a circle with 40 mm diameter was obtained. The non-equiaxial sample was stretched until an ellipse with a major axis of 40 mm and a minor axis of 30 mm was obtained. Before the electrodes were applied, a piece of copper tape was attached outside the circular boundary on the front surface (the surface facing the cameras). The electrode material used was a carbon grease by MG Chemicals. The grease proved to be too viscous and hard to apply in a desired shape so it was mixed with carbon black powder to make it thicker. The resulting mixture consisted approximately of 70 wt% of carbon grease and 30 wt% carbon black powder. Circular electrodes with tracks to the boundary were brushed on using masks as shown in Figure 5.4. The tracks, approximately 1.5 mm wide, were drawn in opposite directions to avoid any unwanted electric field. To get an even thickness of the electrodes the edge of a plastic card was drawn over the electrodes. A speckle pattern was sprayed on the front surface using an airbrush with white acrylic paint. The electrode was covered with a mask when the paint was sprayed on, due to indications from earlier experiments that the paint lowered the conductivity of the electrode. White powder, originally intended as colour pigments for mixing paint, was sprinkled on the electrode to provide a speckle pattern. Finally, the sample was attached on the sample holder described in chapter 4, see Figure 5.5. The back electrode is connected via a piece of copper tape that is attached on one of the arms of the sample holder.

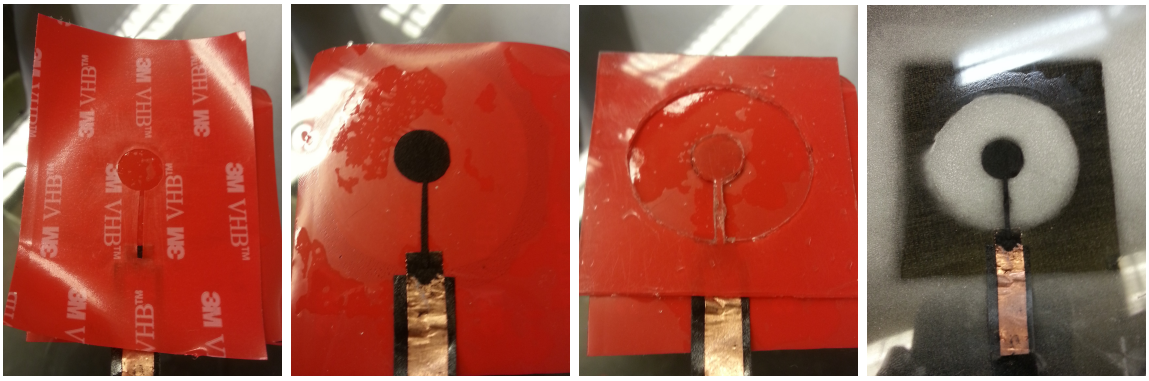

Figure 5.4: The application of electrode and speckle pattern

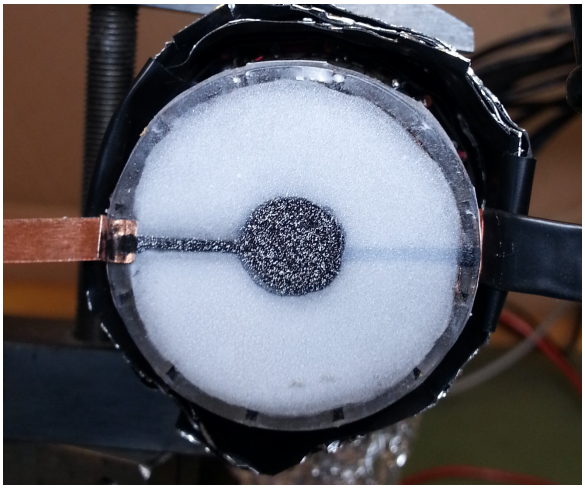

Figure 5.5: Finished sample

Chapter 6

Results and Discussion

6.1 Uniaxial tensile tests

6.1.1 Results

Seven experiments were performed with a strain rate of 5 mm/min, four of which were strained to failure. Only two experiments were performed with a strain rate of 0.06 mm/min. Results from two tests, one at each strain rate, which are considered to be representative of the tests, are shown. The initial length was determined to be approximately 12 mm. To see results from all tests, see Appendix A.

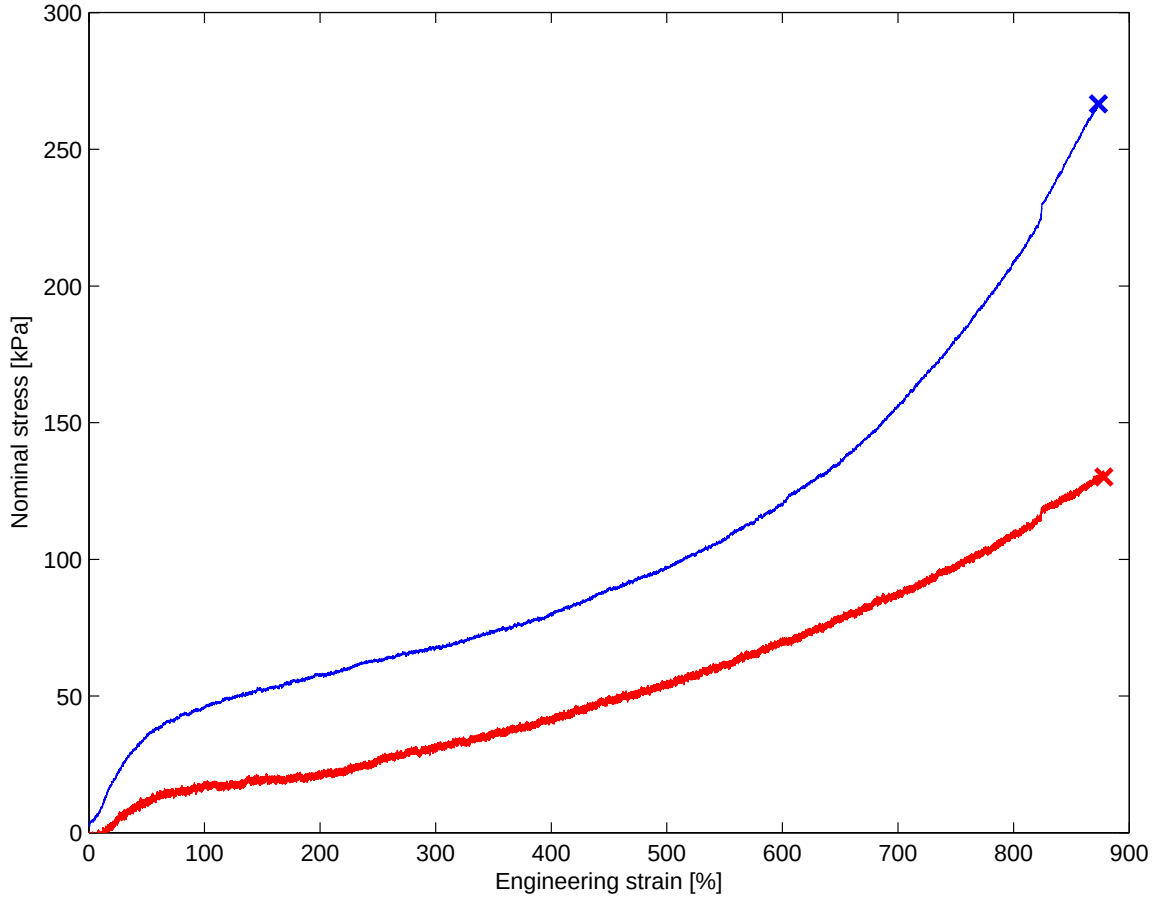

Figure 6.1: Displacement controlled uniaxial tensile tests. The blue graph shows a test with a strain rate of 0.42 s^{-1} and the red graph a strain rate of 0.005 s^{-1}. The 'x' marks where the sample failed.

6.1.2 Discussion

The uniaxial tensile tests performed at the strain rate of 5 mm/min showed little variation and the results seem repeatable. There was, however, a significant variation on the point of failure, one sample failed at 740% for instance. A probable cause of this variation could be the way the samples were cut. Using a scissor did not always result in clean cuts and could have caused micro cracks.

Because only two samples were tested at the slower displacement rate, the results are to be considered preliminary and further testing is needed to conclude if the results are repeatable.

The tests seem fairly consistent with the literature, for instance, compared to the experiments made by Hossain et al. (2012) [14].

We can see that it is possible to distinguish three different phases in the stress-strain response. First, the material shows a steep gradient which reduces after about 50 % strain for both strain rates. This is followed by an almost linear segment until about 325 % for the fast strain rate and 175 % for the slow strain rate. In the final phase, we see a strain hardening until failure, which is more pronounced for the fast

rate.

6.2 WAXS

6.2.1 Results

Although SAXS experiments were also performed, only the WAXS results are presented. This is because the WAXS data contains the same information as the SAXS data, but detects some additional structure at wide angles.
The results are shown either as 2D images or as profiles. Two types of profiles are used, radial profiles and azimuthal profiles. The radial profiles show the variation along a radius defined by its length, azimuthal section and center point. The azimuthal angle is an angle around the z-direction (direction of the incident beam) which is positive counter-clockwise and starting from the negative vertical direction. Azimuthal profiles show the variation along an arc defined by a starting and ending angle and a radial section. The long axis of the sample (perpendicular to the roll length) is stretched in the vertical direction.

Figure 6.2 shows two images with example WAXS patterns, one at an unstrained state and one just before the sample failed at 780 % axial strain. In Figure 6.3 we see the evolution of two radial profiles with increasing strain. One at a 90 ° degree azimuth angle and one at 180 °.

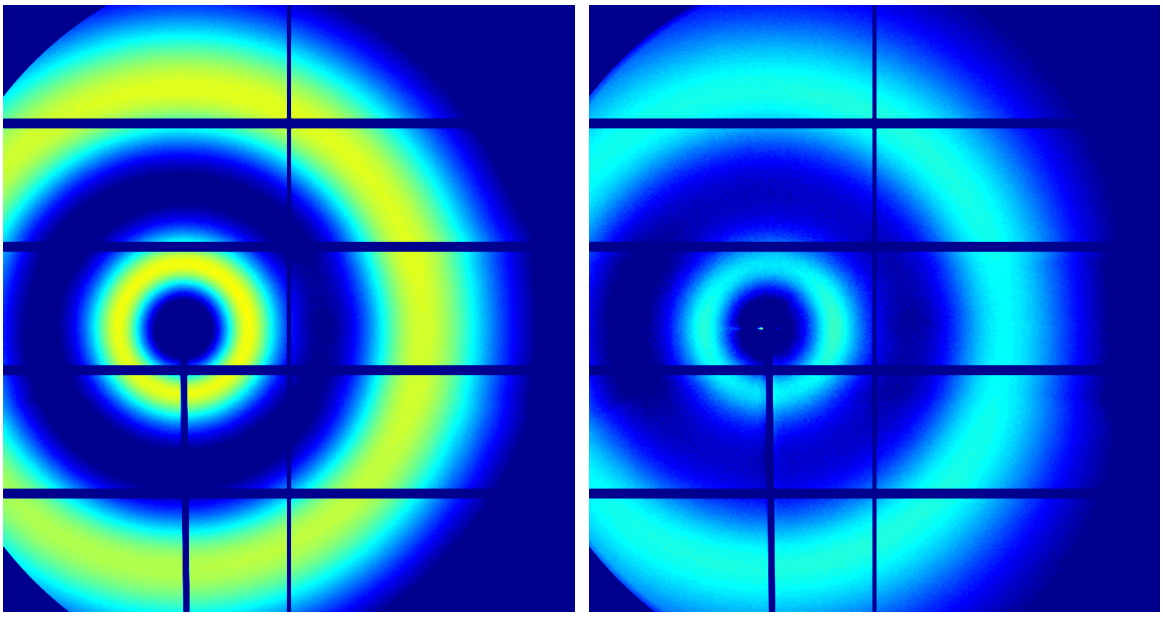

(a) 0 %

(b) 780 %

Figure 6.2: WAXS images for the VHB 4910 unstrained and strained.

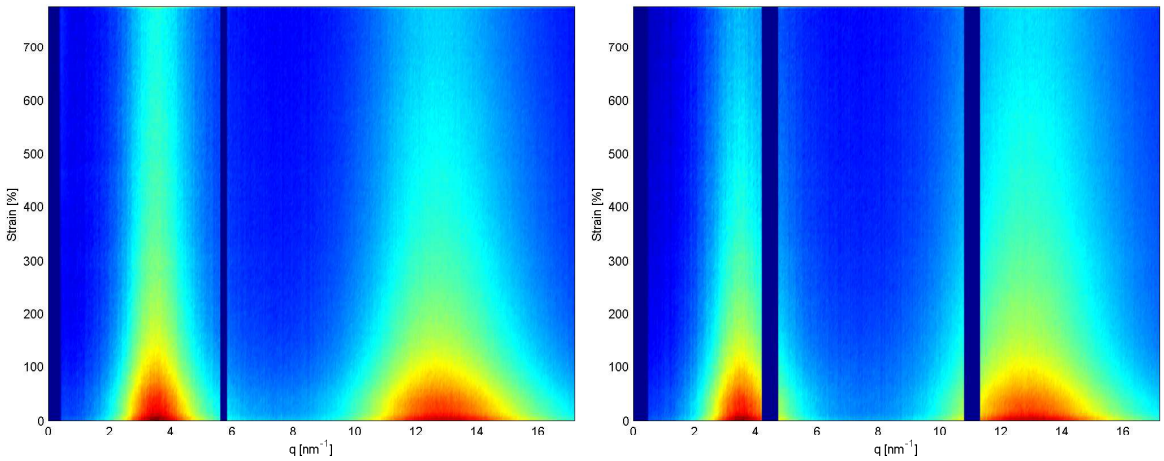

(a) 90 ° (b) 180 °

Figure 6.3: Evolution of two radial profiles.

To quantify any changes to the two WAXS peaks, Gaussian distributions were fitted to each of the peaks. The peaks were fitted separately where the first peak was fitted over the data in a q-range of 0-7.5 nm^{-1} and the second peak over 7.5-17 nm^{-1}. Data points with an intensity below 0.3 a.u. were ignored for the unstrained sample and data points below 0.12 a.u. were ignored for the sample at 780 % strain. Three fittings at different azimuth angles are shown in Figure 6.4 and Figure 6.5, both for the unstrained sample and the sample at 780 % axial strain.

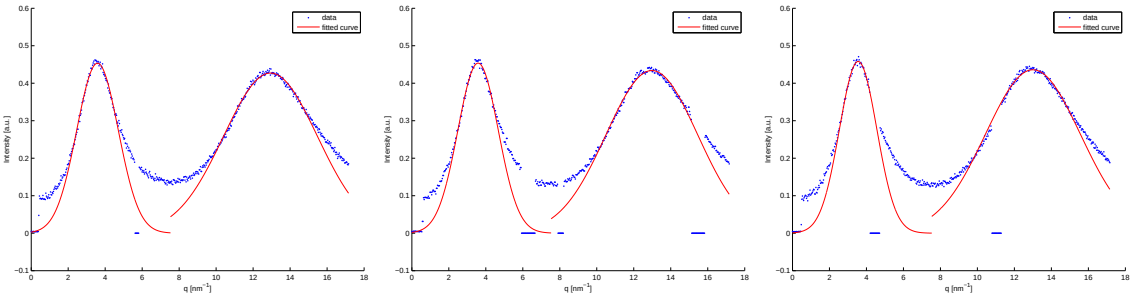

(a) 90 ° (b) 135 ° (c) 180 °

Figure 6.4: Gaussian fits at three azimuth angles for the unstrained sample

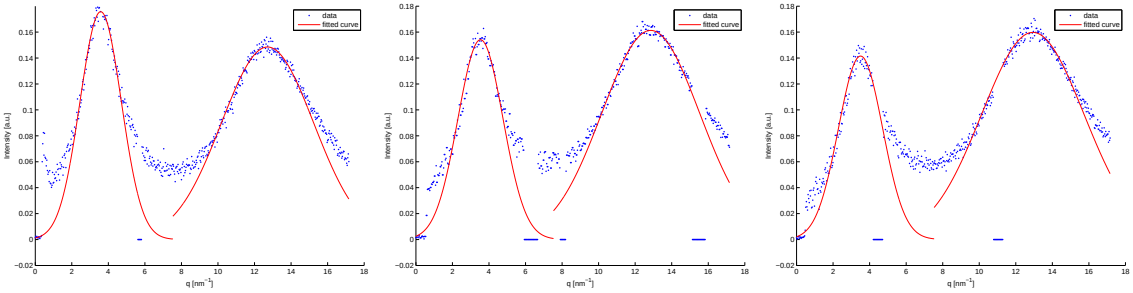

(a) 90 ° (b) 135 ° (c) 180 °

Figure 6.5: Gaussian fits at three azimuth angles at 780 % strain

The root mean squared error (RMSE) is used to quantify how good the fittings are. In Figure 6.6 the RMSE is plotted as a function of azimuth angle:

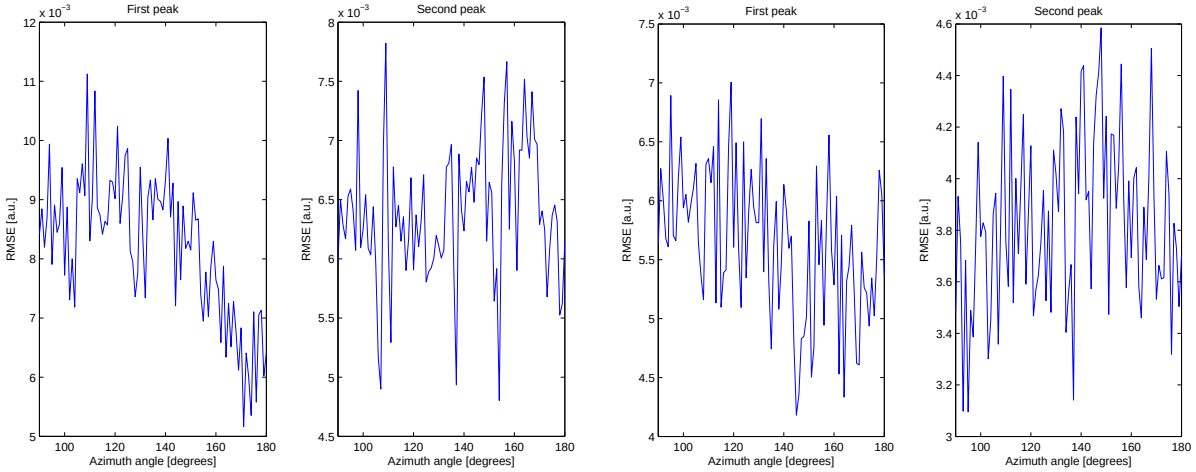

(a) 0 % (b) 780 %

Figure 6.6: Root mean squared error of the Gaussian fits

To assess the anisotropy of the orientation distribution function and how it changes with strain , the variation of the magnitude of the two peaks as a function of azimuth angle, given by the Gaussian fits, is shown in Figure 6.7.

Furthermore the change in the scattering lenghts, which is indicative of strain, are assessed through the change in the q-value of the peak of the Gaussian fits; these are presented in Figure 6.8 and summarised in Table 6.1.

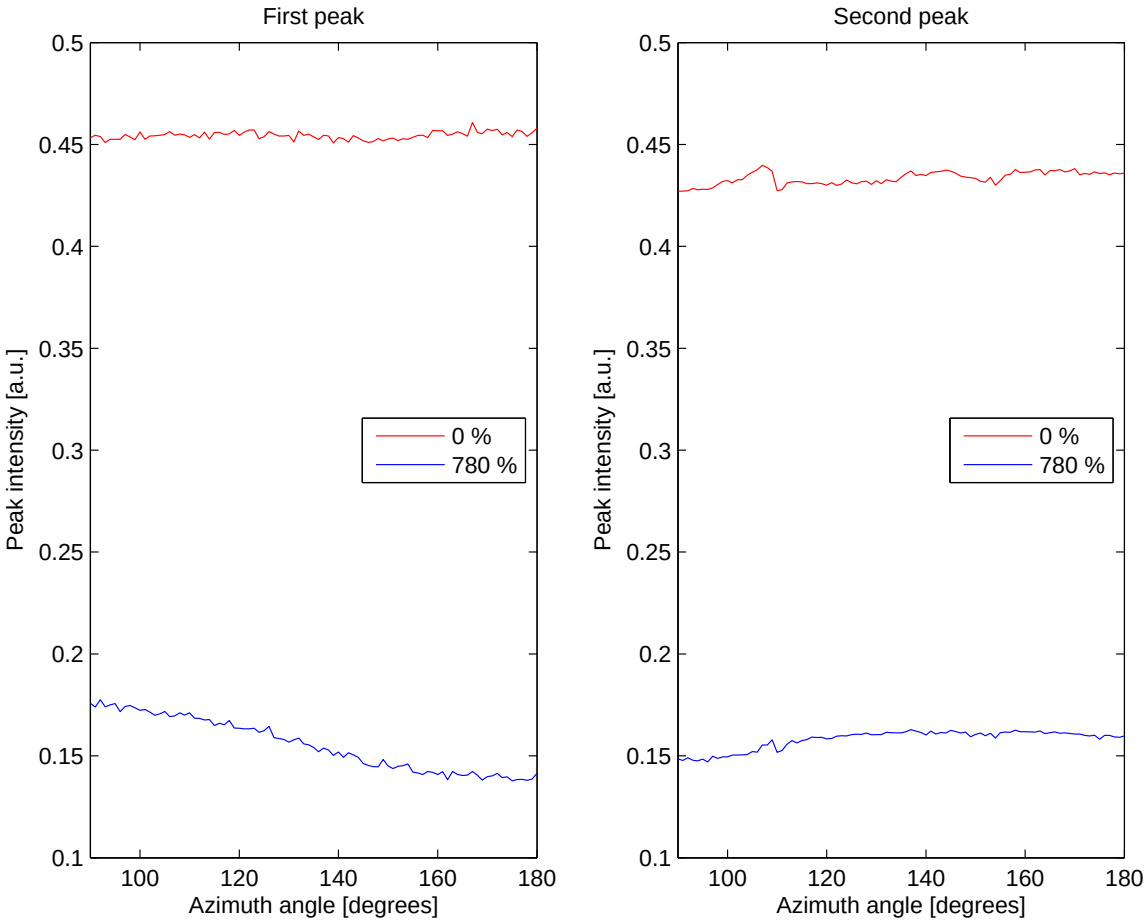

Figure 6.7: Azimuthal profiles for peak intensity

The centroid of the Gaussian fits as a function of azimuth angle:

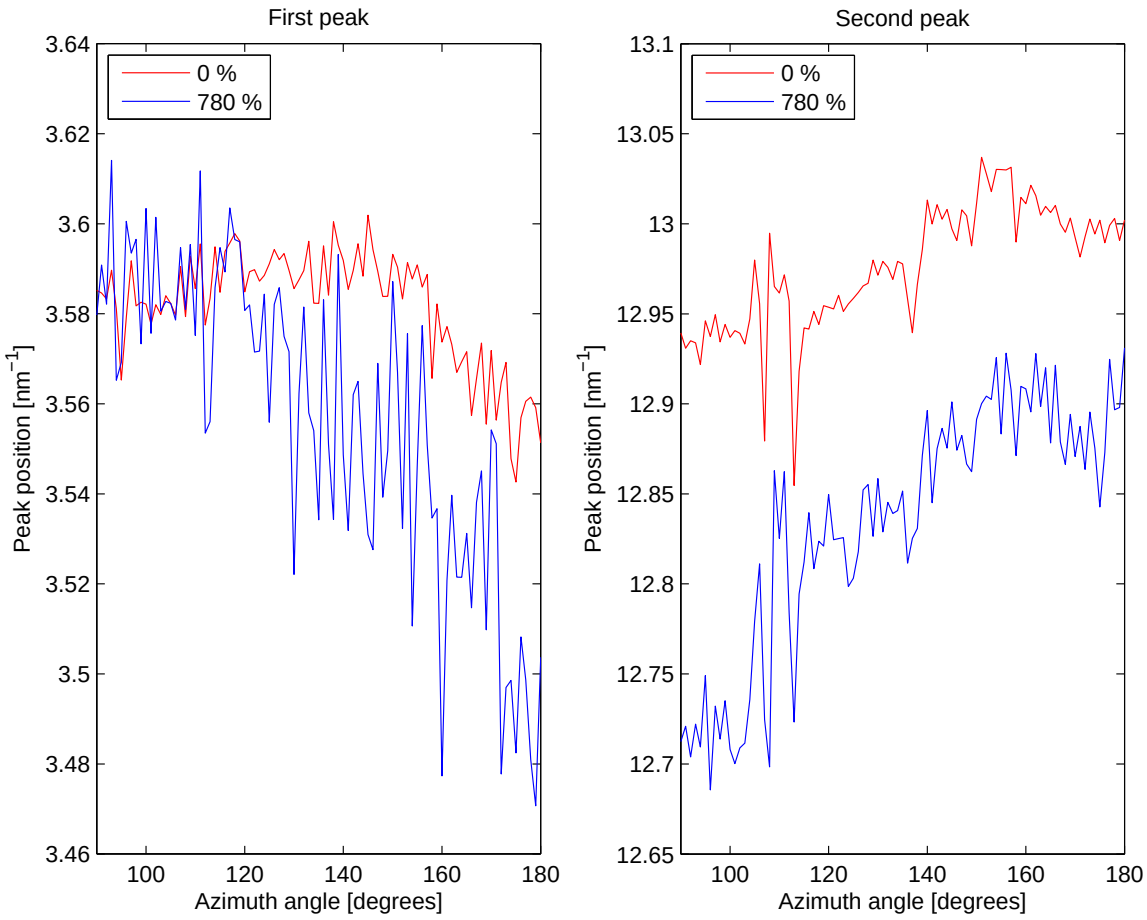

Figure 6.8: Azimuthal profiles for peak position

The centroids of the two peaks correspond to the d-spacings:

Table 6.1: D-spacings calculated using Equation 3.6. Both for the unstrained and strained sample as well as in two directions, parallel (180 °) and perpendicular (90 °) to the loading direction.

Azimuth	First peak	Second peak
90 °	1.753 nm	0.486 nm
180 °	1.769 nm	0.483 nm

(a) 0 % strain

Azimuth	First peak	Second peak
90 °	1.755 nm	0.494 nm
180 °	1.793 nm	0.486 nm

(b) 780 % strain

Strains calculated using Equation 3.8:
First peak:
$\varepsilon_{90^\circ} = 0.0015$
$\varepsilon_{180^\circ} = 0.0136$
Second peak:

$\varepsilon_{90^\circ} = 0.0179$
$\varepsilon_{180^\circ} = 0.0055$

The parameter related to the width of the Gaussian fits as a function of azimuth angle is presented in Figure 6.9; this gives an idea to the variation of strains about the central value.

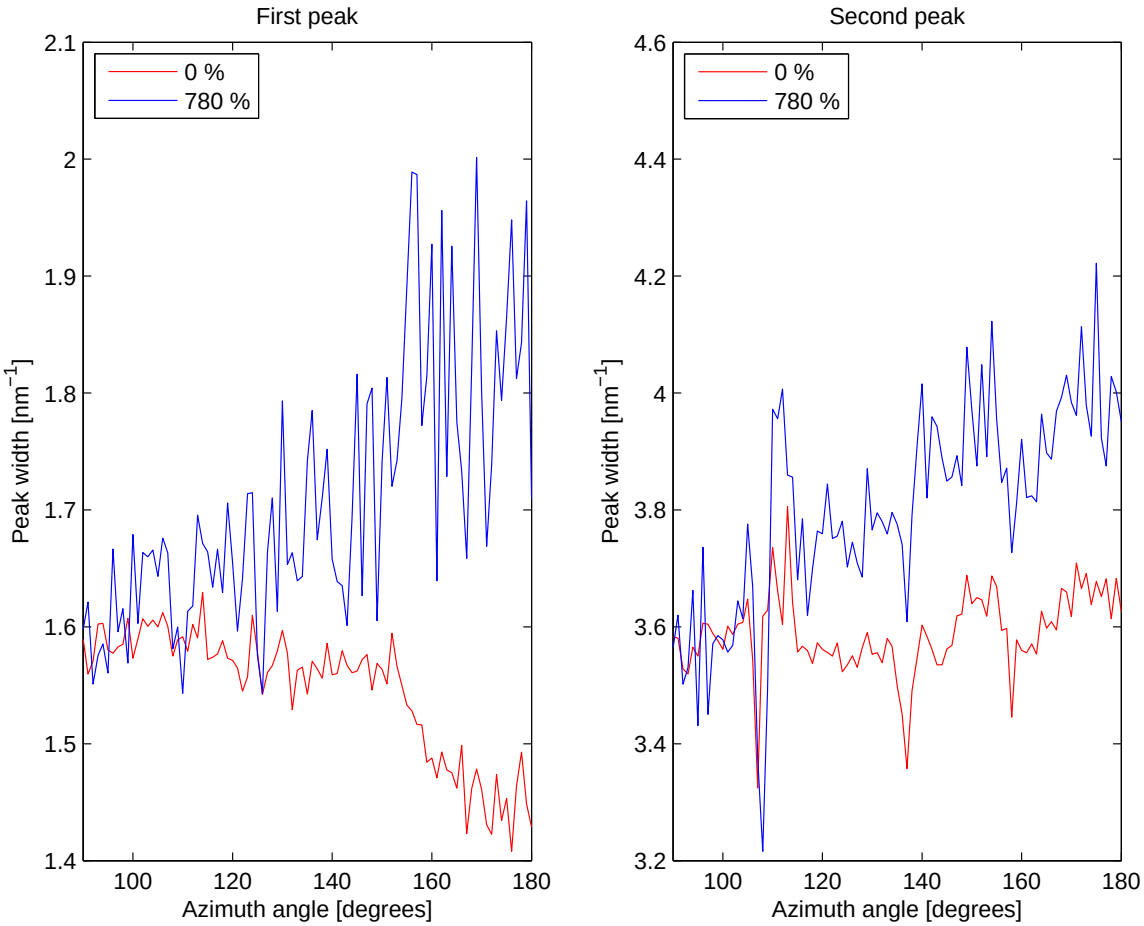

Figure 6.9: Azimuthal profiles for peak width

To investigate whether electrodes would have an influence on the WAXS pattern for future electromechanical testing, a comparison is made between a sample of VHB 4910 without an electrode coating and sample with an electrode coating. Since the WAXS is the sum of the scattering from the elastomer and the electrode material, it is possible to subtract the scattering from the elastomer from the sample with the electrode coating. In Figure 6.10 and Figure 6.11, 2D images and radial profiles are shown with and without electrodes as well as the electrode contribution by itself by subtracting the WAXS pattern without electrodes from the WAXS pattern with electrodes.

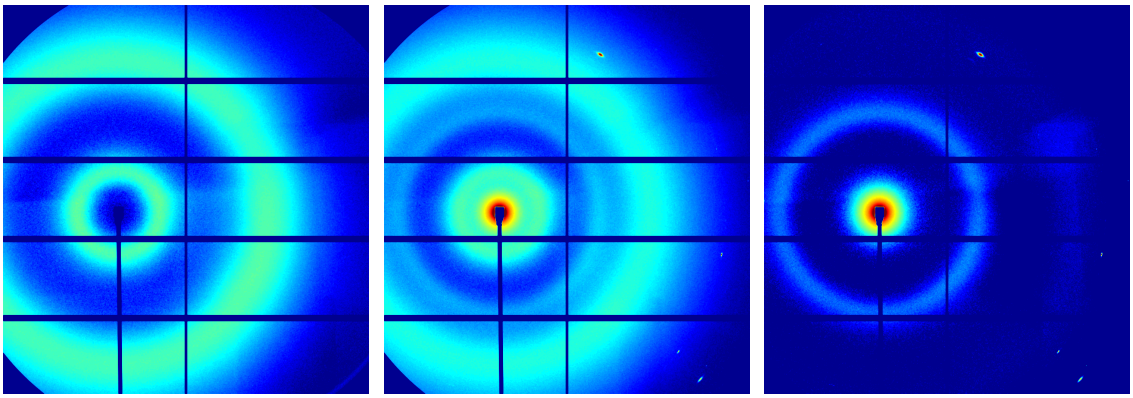

(a) (b) (c)

Figure 6.10: 2D images showing the influence of the electrode coating. a) Without electrode coating. b) With electrode coating. c) a subtracted from b.

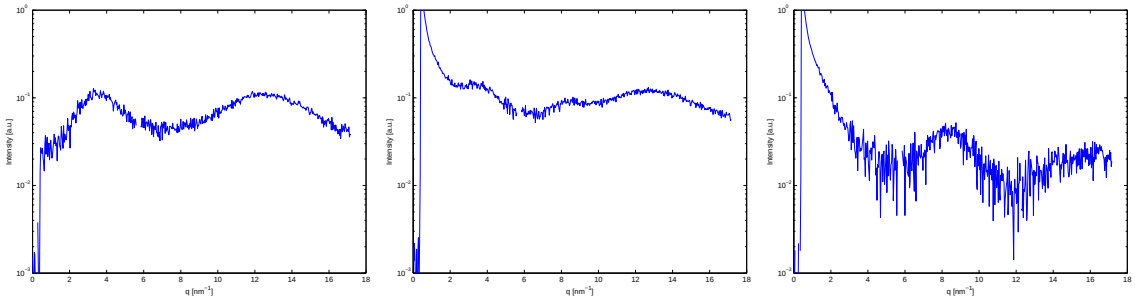

(a) (b) (c)

Figure 6.11: Radial profiles at 90 ° degree azimtuh angle showing the influence of the electrode coating. a) Without electrode coating. b) With electrode coating. c) a subtracted from b.

6.2.2 Discussion

We see from Figure 6.2a that the scattering from the VHB 4910 sample produces two broad peaks, commonly referred to as halos. After straining the sample, the scattering pattern looks almost unchanged. However, the two halos seem to get slightly anisotropic in intensity.

In Figure 6.3 where the evolution of the two peaks are shown with increasing strain, the only apparent change is the decrease in intensity due to the reduction in thickness. In order to quantify any changes to the peaks a simple one term Gaussian fit was made to each of the peaks. The fits were made on radial profiles over an azimuthal range between 90 ° and 180 ° to be able to study any anisotropy. In Figure 6.4 and Figure 6.5, where the Gaussian fits are shown together with the scattering data, we see that the tails of the peaks are not well fitted. However, the fittings were deemed sufficient to identify any changes to the peaks.

As seen earlier from the 2D images there is a grid in the detector where no data

are recorded, which could cause bad fittings at certain azimuth angles. The root mean squared error is used to check if so that the fits were good over the whole azimuthal range.

In Figure 6.7 we see that that the two peaks are isotropic (no change with azimuth angle) at the unstrained state, but at 780 % strain there is a noticeable anisotropy, specially for the first peak.

In Figure 6.8 where the centroid of the peaks are plotted, we can see that there is a noticeable peak shift when the sample is strained. Interestingly, the peak positions are not constant with azimuth angle for the unstrained sample which suggests that the material is slightly anisotropic due to its manufacturing. Unstrained, the d-spacing for the first halo is larger perpendicular to the roll length, while the d-spacing for the second halo is slightly larger parallel to the roll length. When comparing the strained with the unstrained WAXS pattern we see that for the first halo, the largest peak shift is parallel to the loading direction, while for the second halo, the shift is larger perpendicular to the loading direction. The strains calculated show that the biggest strain is for the second halo perpendicular to the loading direction of almost 2 %.

In Figure 6.9, where the widths of the peaks are plotted we see that both peaks get wider when the sample is strained. The width is increasingly larger with azimuth angle and is widest in the loading direction. We also see that for the first peak the width is anisotropic even for the unstrained sample.

The influence of the electrode material to the diffraction pattern is shown in Figure 6.10 and Figure 6.11. We see that there is significant scattering from the electrode material. The electrode material has a ring which is approximately between the two halos of the VHB 4910 sample and there is also strong scattering at small q-values which obscures the left tail of the first halo. Unfortunately, this means that evaluating the structure of VHB 4910 when it is electrically loaded can be a bit challenging. However, it is possible to subtract the scattering from the electrode material if it can be identified properly.

6.3 DIC

Two test were performed with the simultaneous DIC and circular force measurements, one with a sample with equiaxial pre-strain of 300 % and one with a sample with 300 % and 200 % pre-strain in the horizontal and vertical direction. The results and discussion from the DIC measurements are presented first and the results and discussion for the force measurements are presented separately in the following section.

6.3.1 Results

Like the results from the WAXS measurements, the results here are presented as 2D images, radial profiles or azimuthal profiles. However, here the azimuth angle is zero at the positive horizontal direction (going left to right). The center point is determined as the point where the displacement in the horizontal and vertical direction are

at their lowest values.

Figure 6.12 shows two photos of the sample when it is unloaded and when 5 kV is applied. In Figure 6.13 and Figure 6.14 the radial displacement and the thickness displacement are plotted for both samples at 5 kV.

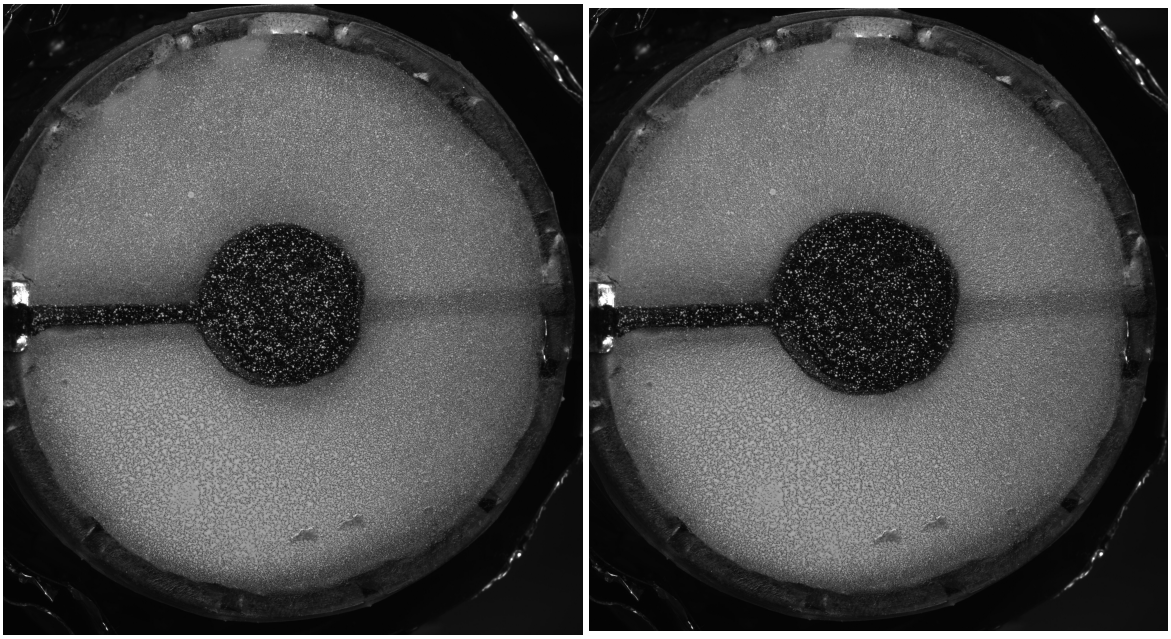

(a) 0 kV (b) 5 kV

Figure 6.12: Photos before and after application of voltage.

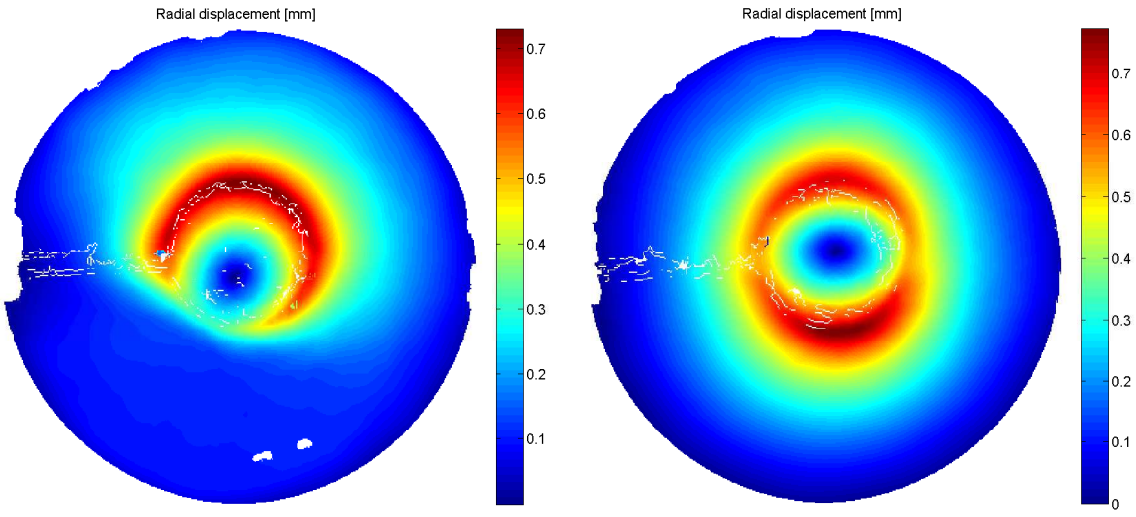

(a) (300%,300%) (b) (300%,200%)

Figure 6.13: Radial displacement for the two pre-strains at 5 kV

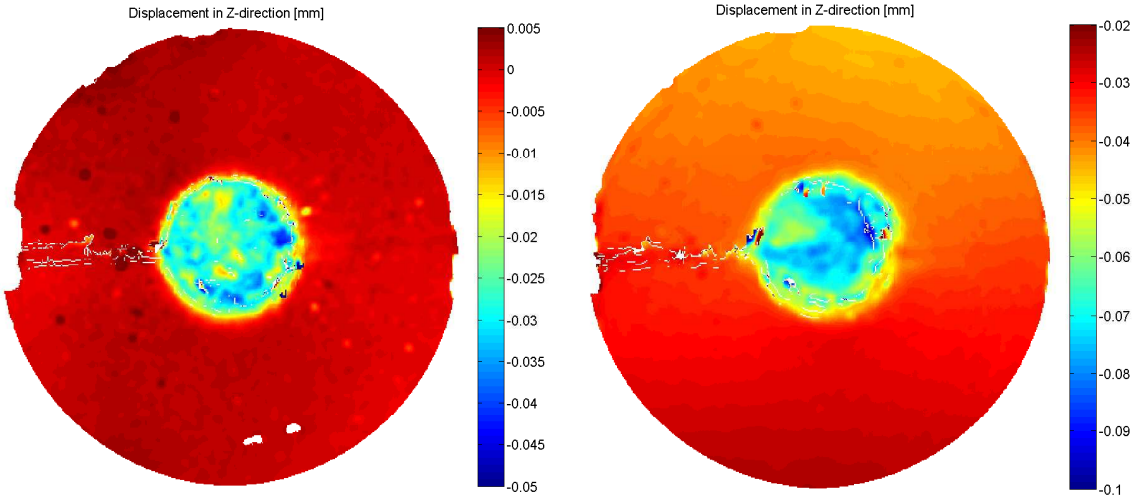

(a) (300%,300%) (b) (300%,200%)

Figure 6.14: Displacement in the thickness direction for the two pre-strains at 5 kV

The principal strains and principal directions given by Equation 3.18 are shown in Figure 6.15 and Figure 6.17 for each sample. The thickness strain calculated with (a) Equation 3.23 and (b) Equation 3.29 are shown for each sample in Figure 6.16 and Figure 6.18.

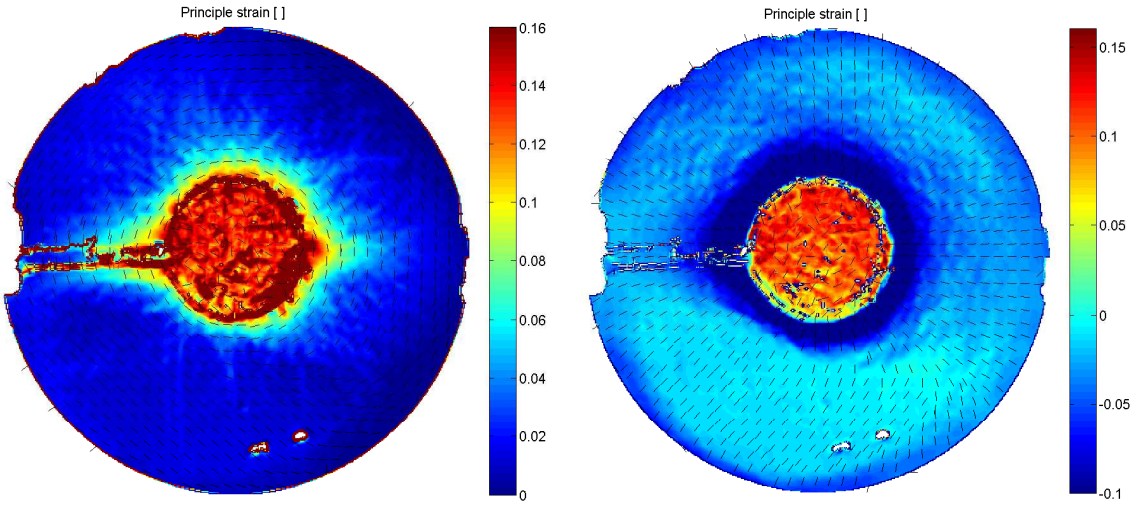

(a) (b)

Figure 6.15: Principal strains and principal strain directions for the sample with (300%,300%) pre-strainat 5 kV.

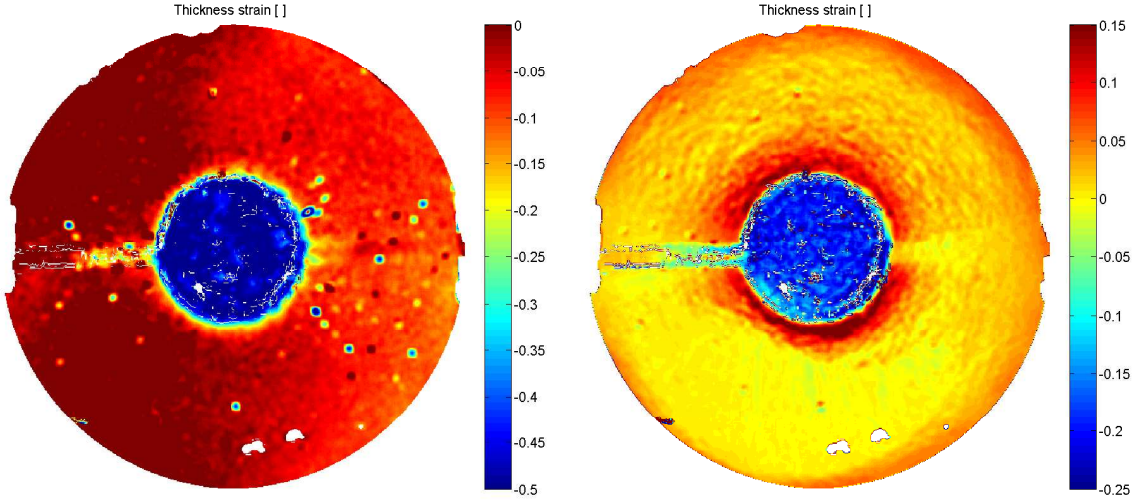

(a) From DIC displacement (b) Calculated using isochoric deformation

Figure 6.16: Thickness strain field at 5kV for the sample with (300%,300%) pre-strain.

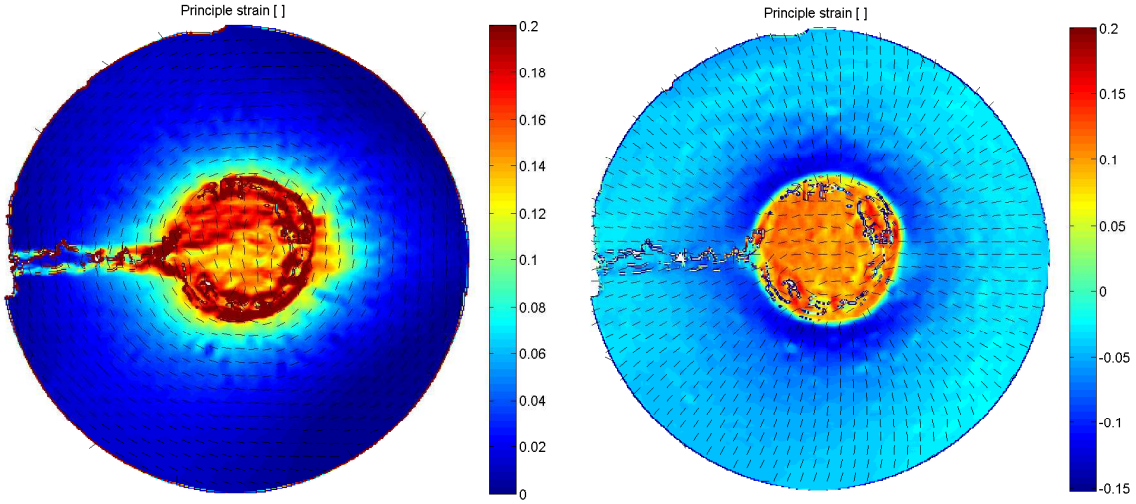

Figure 6.17: Principal strains and principal strain directions for the sample with (300%,200%) pre-strain at 5 kV.

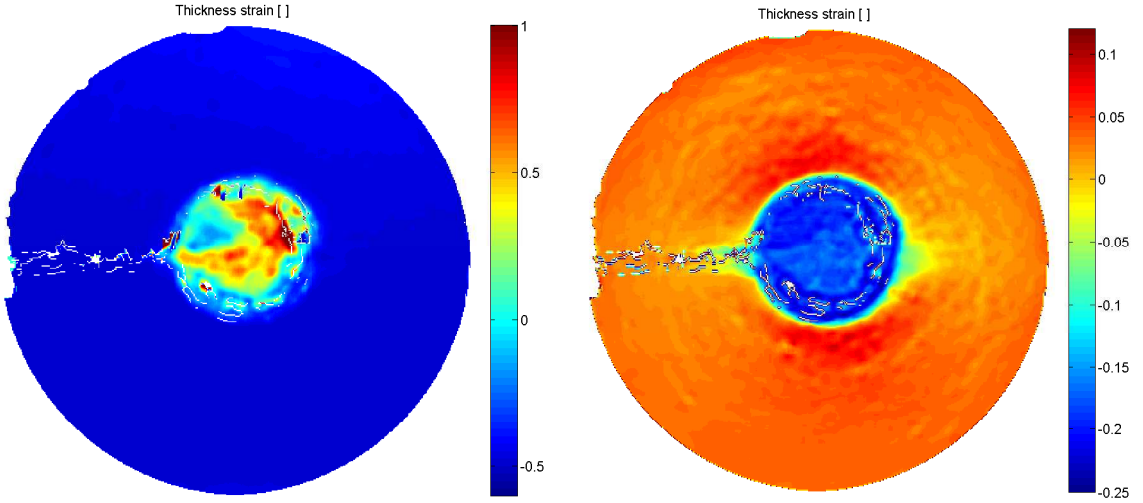

(a) From DIC displacement (b) Calculated using isochoric deformation

Figure 6.18: Thickness strain field at 5kV for the sample with (300%,200%) pre-strain.

To analyse how the thickness strain varies radially and how it evolves with different applied voltages, radial profiles at a 90 ° azimuth angle for the sample with equiaxial pre-strain are shown in Figure 6.19.

As a way to validate the thickness strain calculated using the displacement from the DIC measurements, the resulting Jacobian is shown in Figure 6.20 as a radial profile at a 90 ° azimuth angle.

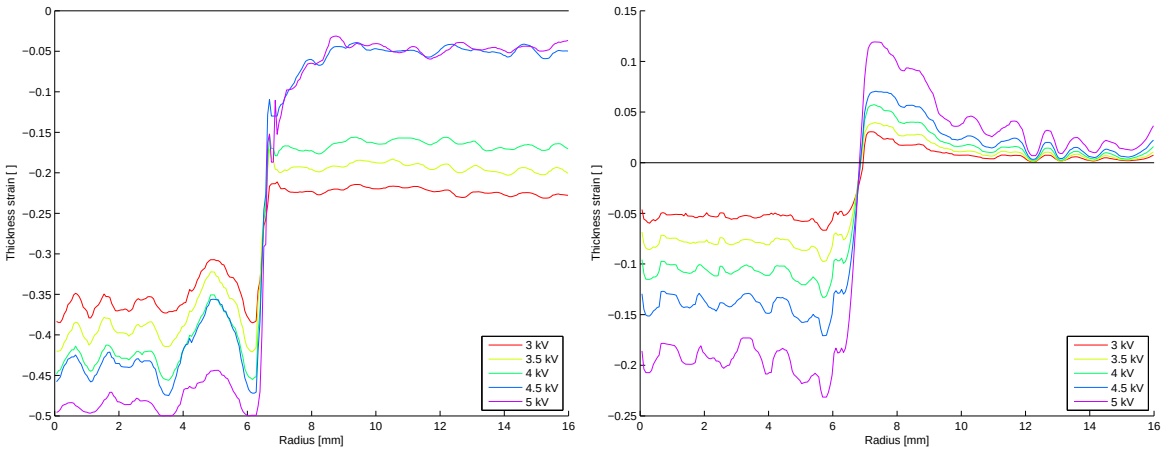

(a) From DIC displacement (b) Calculated using isochoric deformation

Figure 6.19: Thickness strain radial profiles at 90 ° degrees azimuth angle for the sample with (300%,300%) pre-strain.

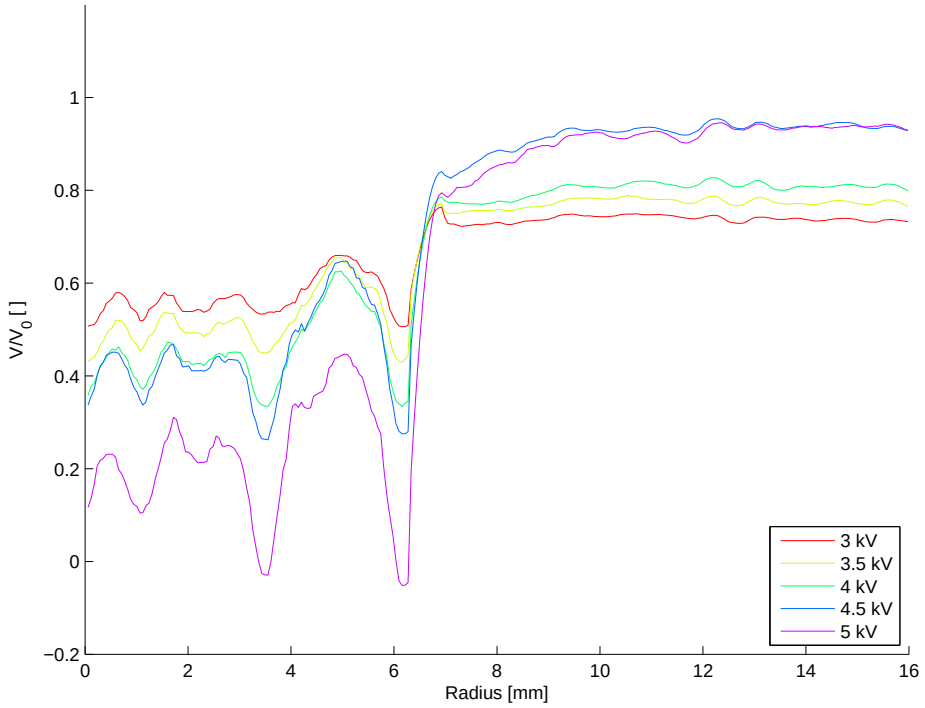

Figure 6.20: Profiles of the Jacobian from the thickness strain calculated from the DIC displacement for the sample with (300%,300%) pre-strain.

6.3.2 Discussion

The major conclusion from the DIC measurements on the equi-axially pre-strained sample is that the different fields do not show axi-symmetry, as one would expect. There are a number of explanations for this. It is important to note that the boundary may not be considered rigid as they consists of flexible arms. The copper tape that was used to connect the two electrodes probably constrained the movement of the two arms that they were attached to. This could explain the higher strains in the horizontal direction seen in Figure 6.15a. Another cause for the higher strain in the horizontal direction could be due to electric fields between the circular electrodes and the paths on opposite side. Another source of error is that the pre-strain was not perfect, which is believed to be the major reason as to why the results were not axi-symmetric.

We see from the photos in Figure 6.12 that the electrode is not perfectly circular, which could also have an effect on the results.

The sample with (300%,200%) pre-strain show more reasonable results. The anisotropy seen in Figure 6.13b shows that the displacement is larger in the direction with lower pre-strain, which is consistent with the literature [1].

It is clear that the thickness strain calculated with the displacement from the DIC measurements is probably not accurate. We see that the whole sample is in compression which suggest that the incompressibility assumption is not fulfilled. This is confirmed by Figure 6.20 where we see that the Jacobian is close to zero in the

electrode area. The displacement in the thickness direction shown in Figure 6.14a seems to be showing a rigid body translation and/or rotation. This is even more evident in Figure 6.14b for the second sample. A slight movement of the cameras or the sample holder would explain the detection of rigid body motion and introduce an error to the DIC measurements. The thickness strain derived from the isochoric assumption seems to give reasonable results. We see in the radial profile from Figure 6.19 that there is a region in the center where the sample is in compression and outside this region the strain abruptly turns into tension and then gradually decreases.

6.4 Boundary forces

6.4.1 Results

The magnitude of the forces at each of the twelve directions for the two pre-strains at 5 kV is shown in Figure 6.21 and the twelve forces averaged and plotted as a function of the applied voltage are shown in Figure 6.22.

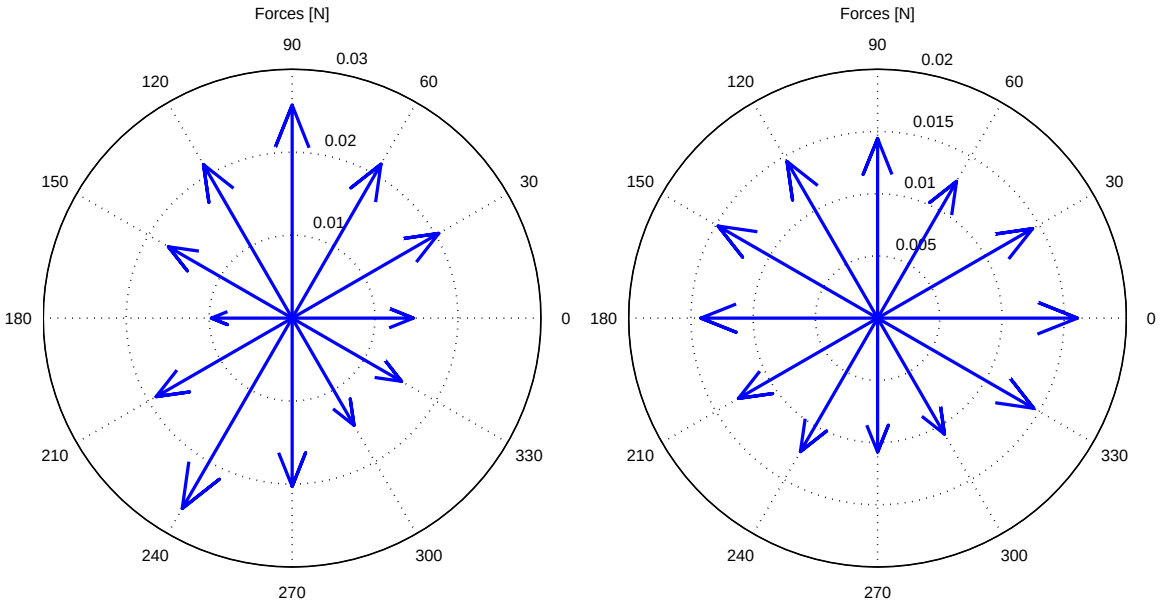

(a) (300%,300%) (b) (300%,200%)

Figure 6.21: Force distribution at 5 kV for the two pre-strains.

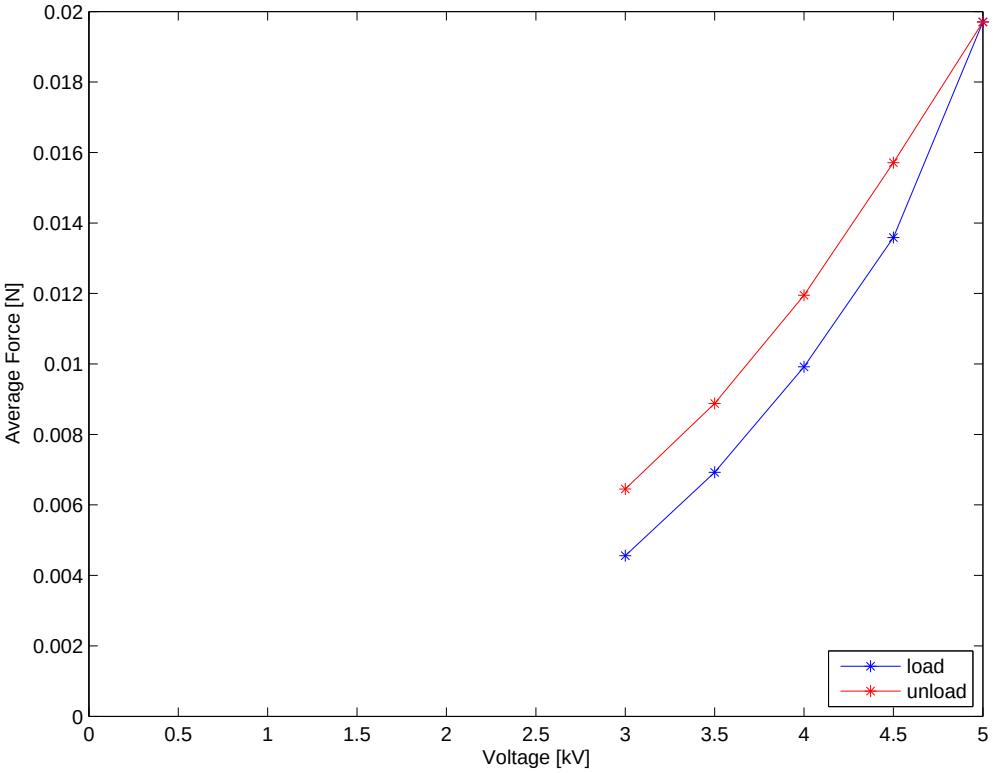

Figure 6.22: The twelve forces averaged versus the electric load.

To see if there is any correlation of the deformation measured by the DIC with the boundary forces, an azimuthal profile of the displacement in the radial direction is compared to the azimuthal profile of the forces and shown in polar plots, see Figure 6.23. The displacement is averaged over a 1 mm radial section near the boundary at each azimuth. Note that the magnitude is not given by the plots and they serve only to compare the shape of the profiles.

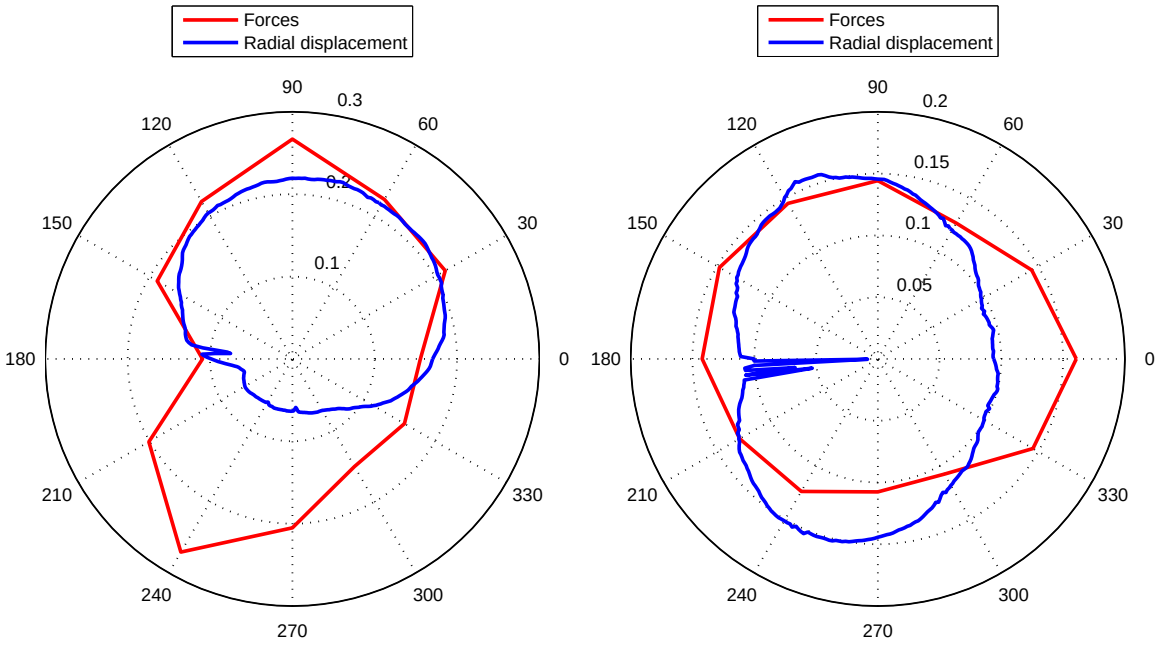

(a) (300%,300%) (b) (300%,200%)

Figure 6.23: Radial displacement azimuthal plots for the two pre-strains at 5kV.

Similar to above, but instead the thickness displacement is compared to the forces, see Figure 6.24. The radial displacement is averaged over a 1 mm radial section near the boundary at each azimuthal.

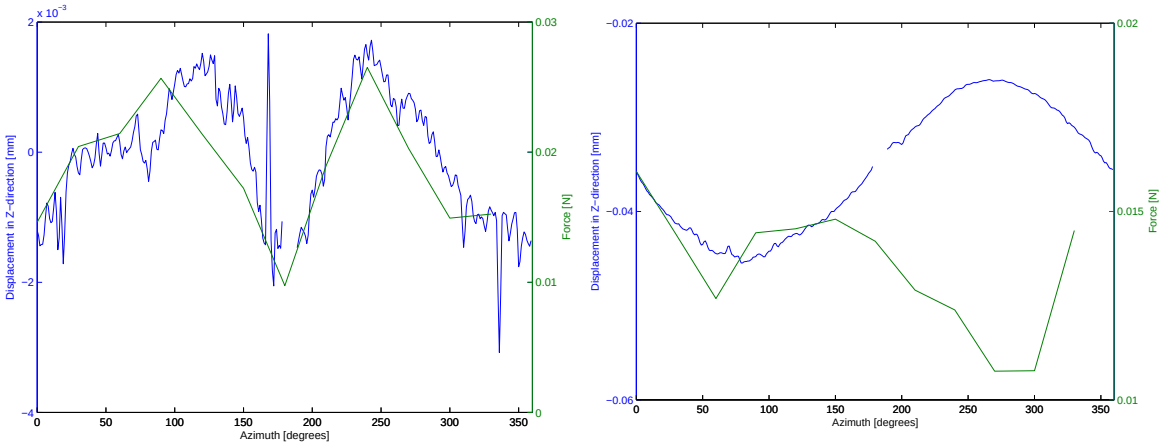

(a) (300%,300%) (b) (300%,200%)

Figure 6.24: Azimuthal plots of the displacement in the thickness direction for the two pre-strains at 5kV.

To see how the radial displacement and the forces evolve with increasing voltage the radial displacement azimuthal profile and the force azimuthal profile are shown at each voltage for the equi-axially pre-strained sample in Figure 6.25 .

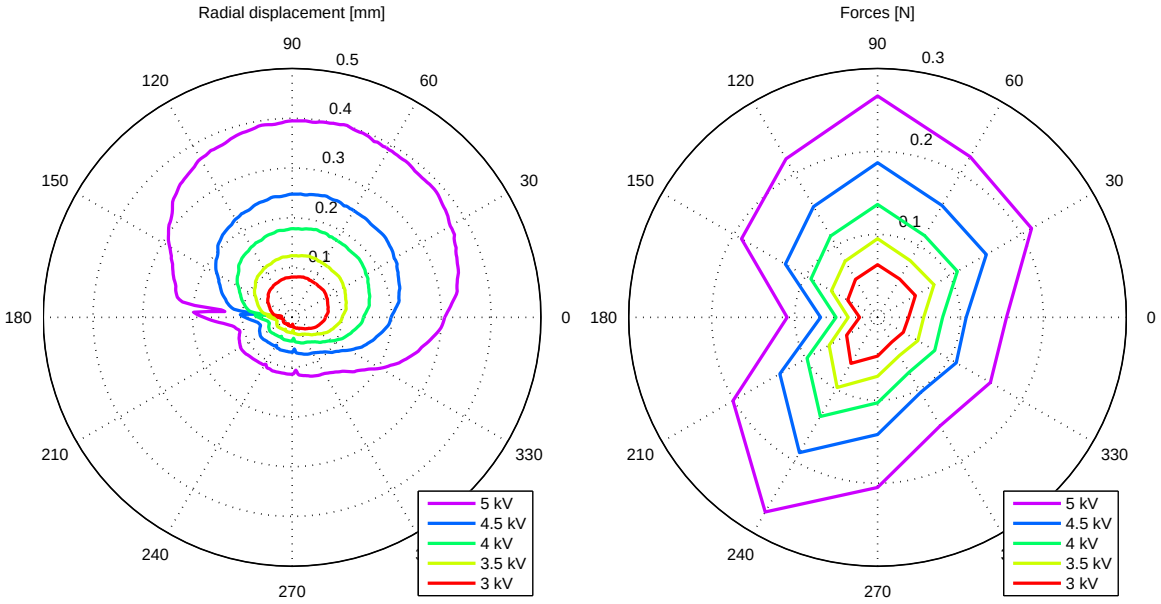

(a) Radial displacement

(b) Forces

Figure 6.25: Evolution with increasing voltage for the sameple with (300%,300%) pre-strain.

6.4.2 Discussion

The force distribution in Figure 6.21 does not show any regular shape. In Figure 6.23, where the force profile is compared to an azimuthal profile of the radial displacement, there does not seem to be any correlation. However in Figure 6.24 there seems to be a correlation between the thickness displacement and the forces in the sample with equiaxial pre-strain, while the other sample does not show any correlation. Whether the arms are measuring something real or are just badly calibrated is hard to say. There are a number of things that could have caused a bad calibration. The arms were calibrated by hanging weights near the edge of the arms, approximately 1 mm from the edge. This was done by eye measurement and there could have been some variation on the position where the weight were hanging and thus induce different amounts of bending moment. There was noticeable creep and non-linearity from the mechanical response of the arms. As the sample was transferred to the sample holder, the sample was pressed against the arms to make it stick. The arms were therefore subjected to relatively large force which could have put each arm at different regions of their non-linear response.

Chapter 7

Conclusion

This thesis has investigated the experimental characterization of a dielectric elastomer, VHB 4910, through different experimental techniques.

The results from the WAXS experiments shows unprecedented results which can be useful in the development of models for VHB 4910. The changes seen when the material is strained is quite subtle and a careful analysis is required to properly interpret the results and relate them to the material structure. The chemical composition of VHB 4910 is largely unknown but a recent article [24] can provide some insight on this matter.

Furthermore, a new experimental method has been developed for this thesis. The method gives the displacement field (and consequently the strain field) as well as the force distribution of an electrically loaded circular sample. This method has several advantages over existing methods found in the literature. The field measurement using DIC allows the study of complex behaviour and reveal potential heterogeneity in the material response that are not revealed in conventional macroscopic measurements. It provides useful information in the interface between the active and inactive areas, for example, it provides the thickness variation over the whole sample, as seen in the results. The method also provides an excellent way of studying anisotropy as the DIC measurements provides information in all directions whereas the force measurements provides the force in twelve radial directions. This allows a way of studying anisotropy from the material itself as well as anisotropy induced by the pre-straining. The force measurements allows models to be fitted with regard to the stresses and not only the strains, as is most common in the literature.

The experiments presented in this thesis are a result of time consuming trials and errors. Despite this, the result indicate that the experimental procedure require some fine tuning in order to acquire better data. The results from the DIC measurements indicate that the boundary conditions are not well defined and therefore, the results are difficult to interpret. Also, the force distribution measured by the twelve-armed device does not seem to be reliable. The problems can however be overcome and future experiments can hopefully provide useful data, as described in the following.

Future work

To identify and deal with possible errors in the experimental procedure a number of precautions can be made. When it comes to the DIC measurements the main sources of errors is believed to be caused during the pre-straining and when the sample is transferred from the pre-straining device to the sample holder. The pre-straining should be performed under more controlled conditions. A few questions that can be useful if answered are:

- How sensitive is the material to the strain rate?
- Is it important that the two directions are strained at equal strain rates?
- Is there any significant relaxation of the pre-straining?
- Is the time between the pre-straining and the time of measurements an important factor?
- Is the pre-straining maintained when the sample is transferred to the sample holder?
- Is the material sensitive to temperature or other environmental factors?

Most importantly, the experiments should be performed several times to check for repeatability.

For the twelve-armed device, the main source of error is believed to be due to the very time-dependent response of the plexi cylinder. It is suggested that another material is chosen with less time-dependant and non-linear response is used.

Bibliography

[1] Paul Brochu and Qibing Pei. Dielectric elastomers for actuators and artificial muscles. In Lenore Rasmussen, editor, *Electroactivity in Polymeric Materials*, pages 1–56. Springer US, 2012. 2, 41

[2] Ron Pelrine and Roy Kornbluh. Introduction: History of dielectric elastomer actuators. In Peter Sommer-Larsen, Federico Carpi, Danilo De Rossi, Roy Kornbluh, and Ronald Pelrine, editors, *Dielectric Elastomers as Electromechanical Transducers*, pages xi – xiii. Elsevier, Amsterdam, 2008. 3

[3] W.D. Callister and D.G. Rethwisch. *Fundamentals of Materials Science and Engineering: An Integrated Approach*. Wiley, 2008. 3, 7

[4] Ronald E. Pelrine, Roy D. Kornbluh, and Jose P. Joseph. Electrostriction of polymer dielectrics with compliant electrodes as a means of actuation. *Sensors and Actuators A: Physical*, 64(1):77 – 85, 1998. Tenth {IEEE} International Workshop on Micro Electro Mechanical Systems. 4

[5] Chong Min Koo. Electroactive thermoplastic dielectric elastomers as a new generation polymer actuators. *Thermoplastic Elastomers*, 2012. 5

[6] Anna Ask. *Modeling and simulation of electro-viscoelastic polymers*. PhD thesis, Lund university, 2013. 5

[7] Bori Kim, Youn Duk Park, Kyoungho Min, Jin Hong Lee, Seung Sang Hwang, Soon Man Hong, Bong Hoon Kim, Sang Ouk Kim, and Chong Min Koo. Electric actuation of nanostructured thermoplastic elastomer gels with ultralarge electrostriction coefficients. *Advanced Functional Materials*, 21(17):3242–3249, 2011. 5

[8] Jean-Sebastien Plante and Steven Dubowsky. Large-scale failure modes of dielectric elastomer actuators. *International Journal of Solids and Structures*, 43(25-26):7727 – 7751, 2006. 5

[9] Ron Pelrine, Roy Kornbluh, Qibing Pei, and Jose Joseph. High-speed electrically actuated elastomers with strain greater than 100%. *Science*, 2000. 6, 7

[10] J. Su, Q. M. Zhang, and R. Y. Ting. Space-charge-enhanced electromechanical response in thin-film polyurethane elastomers. *Applied Physics Letters*, 71(3), 1997. 6

[11] Guggi Kofod, Peter Sommer-Larsen, Roy Kornbluh, and Ron Pelrine. Actuation response of polyacrylate dielectric elastomers. *Journal of Intelligent Material Systems and Structures*, 14(12):787–793, 2003. 6, 7

[12] Samuel Rosset and Herbert R. Shea. Flexible and stretchable electrodes for dielectric elastomer actuators. *Applied Physics A*, 110(2):281–307, 2013. 6

[13] Ravi Shankar, Tushar K. Ghosh, and Richard J. Spontak. Dielectric elastomers as next-generation polymeric actuators. *Soft Matter*, 3:1116–1129, 2007. 7

[14] Mokarram Hossain, Duc Khoi Vu, and Paul Steinmann. Experimental study and numerical modelling of {VHB} 4910 polymer. *Computational Materials Science*, 59(0):65 – 74, 2012. 7, 28

[15] Mokarram Hossain, DucKhoi Vu, and Paul Steinmann. A comprehensive characterization of the electro-mechanically coupled properties of vhb 4910 polymer. *Archive of Applied Mechanics*, 85(4):523–537, 2015. 7

[16] Michael Wissler and Edoardo Mazza. Mechanical behavior of an acrylic elastomer used in dielectric elastomer actuators. *Sensors and Actuators A: Physical*, 134(2):494 – 504, 2007. 7

[17] JoshuaS. Stenzler and N.C. Goulbourne. Effect of polyacrylate interlayer microstructure on the impact response of multi-layered polymers. In Tom Proulx, editor, *Time Dependent Constitutive Behavior and Fracture/Failure Processes, Volume 3*, Conference Proceedings of the Society for Experimental Mechanics Series, pages 241–258. Springer New York, 2011. 7

[18] R.J. Roe. *Methods of X-ray and Neutron Scattering in Polymer Science*. Topics in polymer science. Oxford University Press, 2000. 9, 10, 12

[19] Jens Als-Nielsen and Des McMorrow. *Elements of Modern X-ray Physics*. Wiley, 2011. 10, 11

[20] *The SAXS Guide*. Anton Paar GmbH., 2011. 11

[21] JonathanD. Almer and RobertA. Winholtz. X-ray stress analysis. In Jr. Sharpe, William N., editor, *Springer Handbook of Experimental Solid Mechanics*, pages 801–820. Springer US, 2008. 12

[22] Michael A. Sutton, Jean-Jose Orteu, and Hubert W. Schreier. Image correlation for shape, motion and deformation measurements. Springer US, 2009. 13, 14

[23] J. Engqvist, S.A. Hall, M. Wallin, M. Ristinmaa, and T.S. Plivelic. Multi-scale measurement of (amorphous) polymer deformation: Simultaneous x-ray scattering, digital image correlation and in-situ loading. *Experimental Mechanics*, 54(8):1373–1383, 2014. 22

[24] Fan Fan and Jerzy Szpunar. Characterization of viscoelasticity and self-healing ability of vhb 4910. *Macromolecular Materials and Engineering*, 300(1):99–106, 2015. 46

Appendix A

Tensile tests

The raw data from all tensile tests.